Mantle dynamics of the Andean Subduction Zone from continent-scale teleseismic *S*-wave tomography

Emily E. Rodríguez [1], Daniel Evan Portner [2], Susan L. Beck,[1] Marcelo P. Rocha,[3]
Marcelo B. Bianchi,[4] Marcelo Assumpção [4], Mario Ruiz,[5] Patricia Alvarado,[6]
Cristobal Condori[3,7] and Colton Lynner [8]

[1]*Department of Geosciences, University of Arizona, 1040 E 4th St, Tucson, AZ 85721, USA. E-mail: rodrigueze@email.arizona.edu*
[2]*Earth and Planets Laboratory, Carnegie Institution for Science, Washington, DC, USA*
[3]*Instituto de Geociências, Universidade de Brasília, Brasília, Brazil*
[4]*Centro de Sismologia, Departamento de Geofísica, Instituto de Geofísica, Astronomia, e Ciências Atmosféricas, Universidade de São Paulo, São Paulo, Brazil*
[5]*Instituto Geofísico, Escuela Politécnica Nacional, Quito, Ecuador*
[6]*CIGEOBIO Consejo Nacional de Investigaciones Científicas y Técnicas, Departamento de Geofísica y Astronomía, Facultad de Ciencias Exactas, Físicas y Naturales, Universidad Nacional de San Juan, San Juan, Argentina*
[7]*Universidad Nacional de San Agustín de Arequipa, Perú*
[8]*Department of Earth Sciences, University of Delaware, Newark, DE, USA*

SUMMARY

The Andean Subduction Zone is one of the longest continuous subduction zones on Earth. The relative simplicity of the two-plate system has makes it an ideal natural laboratory to study the dynamics in subduction zones. We measure teleseismic *S* and SKS traveltime residuals at >1000 seismic stations that have been deployed across South America over the last 30 yr to produce a finite-frequency teleseismic *S*-wave tomography model of the mantle beneath the Andean Subduction Zone related to the Nazca Plate, spanning from ∼5°N to 45°S and from depths of ∼130 to 1200 km. Within our model, the subducted Nazca slab is imaged as a fast velocity seismic anomaly. The geometry and amplitude of the Nazca slab anomaly varies along the margin while the slab anomaly continues into the lower mantle along the entirety of the subduction margin. Beneath northern Brazil, the Nazca slab appears to stagnate at ∼1000 km depth and extend eastward subhorizontally for >2000 km. South of 25°S the slab anomaly in the lower mantle extends offshore of eastern Argentina, hence we do not image if a similar stagnation occurs. We image several distinct features surrounding the slab including two vertically oriented slow seismic velocity anomalies: one beneath the Peruvian flat slab and the other beneath the Paraná Basin of Brazil. The presence of the latter anomaly directly adjacent to the stagnant Nazca slab suggests that the plume, known as the Paraná Plume, may be a focused upwelling formed in response to slab stagnation in the lower mantle. Additionally, we image a high amplitude fast seismic velocity anomaly beneath the Chile trench at the latitude of the Sierras Pampeanas which extends from ∼400 to ∼1000 km depth. This anomaly may be the remnants of an older, detached slab, however its relationship with the Nazca–South America subduction zone remains enigmatic.

Key words: South America; Seismic tomography; Dynamics of lithosphere and mantle.

1 INTRODUCTION

Improvements in global seismic instrument coverage have provided increasingly higher resolution models of the seismic velocity structure of subduction zones. New models reveal a complex image of subduction, illuminating a mantle that is heterogeneous with fast and slow velocity anomalies that surround and are in contact with subducting slabs (e.g. Schmandt & Lin 2014; Tao *et al.* 2018). The heterogeneous image of the mantle has incited interest in the influence of non-slab anomalies on mantle flow dynamics which may play critical roles in global processes of material recycling and heat transport (e.g. Faccenna *et al.* 2013; Chang *et al.* 2016; Hu *et al.* 2018).
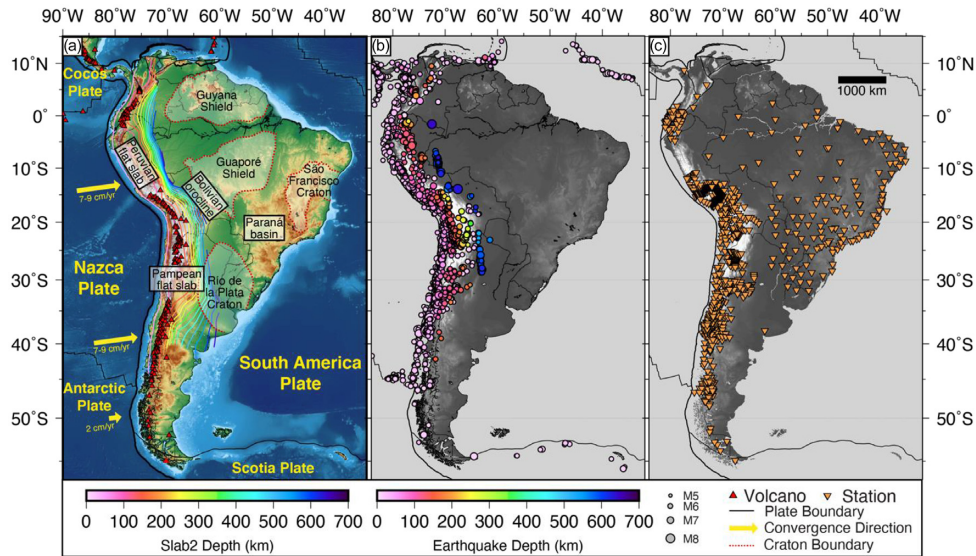
Figure 1. (a) Tectonic map of South America. Black lines denote major plate boundaries (Coffin *et al.* 1998) and convergence velocity (DeMets *et al.* 2010). The dashed regions correspond to the surface expression of cratons (adapted from Rocha *et al.* 2011 and Rapela & Baldo 2014). Active Holocene volcanoes are shown as triangles (Siebert *et al.* 2011). Contours show the Slab2 model of the Nazca slab (Hayes *et al.* 2018). (b) Location of >*M*5 earthquakes from 1960 until 1 January 2020 (NEIC-USGS, USA Earthquake catalogue 2020). Colour scale denotes the hypocentral depth, see colour scale within figure. (c) Inverted triangles show the location of stations used within our model.

The Andean Subduction Zone is a long-lived and continuous system with ongoing subduction since at least the Mesozoic (e.g. Mégard 1987; Somoza & Ghidella 2012; Horton 2018). The subduction zone is characterized by the eastward subduction of the oceanic Nazca Plate beneath the continental South American Plate for ∼7000 km along strike (Fig. 1a). Convergence along most of the margin is relatively uniform at ∼7–9 cm yr^{-1} at an azimuth of ∼71–78° (DeMets *et al.* 2010). North of 2°S, convergence slows to 5.8 cm yr^{-1} (Trenkamp *et al.* 2002). The spatial and temporal scale and relative simplicity of the Andean Subduction Zone makes it ideal for assessing the role of supraslab mantle anomalies on the dynamics of the subduction system.

Global body wave tomography models image a continuous Nazca slab from ∼10°N to 35°S beneath South America (e.g. Bijwaard *et al.* 1998; Li *et al.* 2008; Fukao & Obayashi 2013; Lu *et al.* 2019). The depth extent into the lower mantle and the morphology of the slab are difficult to discern between models owing to a broadening of resolution with depth. Many global models show some indications of the Nazca slab extending into the lower mantle and stagnating beneath northern Brazil at ∼1000 km depth and subducting at a normal dip of ∼30° to the south. Regionally focused teleseismic tomography studies echo such behavior with improved resolution of the slab, revealing a more complicated slab geometry. Such models show sharp transitions from flat to normal subduction angles both along-strike and downdip (e.g. Scire *et al.* 2016, 2017; Portner *et al.* 2020), the existence of tears and holes in the slab (Pesicek *et al.* 2012; Scire *et al.* 2016; Portner *et al.* 2017, 2020) and the interaction of the slab with sub- and supraslab velocity anomalies (e.g. Scire *et al.* 2016, 2017; Portner *et al.* 2017; Celli *et al.* 2020). The size and full geometry of many of these anomalies remain ambiguous, particularly in teleseismic *S*-wave studies which have been previously limited in their footprint in South America.

We improve on existing *S*-wave velocity models of the South American mantle by achieving high-resolution images at the continent scale. Our results expand both laterally and in depth the *S*-wave teleseismic tomography model of Scire *et al.* (2016), which covered

the upper mantle beneath southern Perú and northernmost Chile and Bolivia. Our final model also complements the SAM5_P_2019 teleseismic *P*-wave velocity model (Portner *et al.* 2020), which incorporated the same seismic stations and model parametrization as this study. Our new teleseismic finite-frequency *S*-wave model of South America takes advantage of more than 30 yr of seismic data collection across South America with a composite seismic station array consisting of >1000 stations. By combining this data into a single tomographic model, we are able to provide a high-resolution image of the entire subduction system and the interactions of the slab with the surrounding mantle. We provide a new context for understanding previously enigmatic seismic anomalies such as the Paraná plume and a relic slab fragment.

2 METHODS AND DATA

2.1 Data

We measure the relative traveltime residuals of teleseismic *S* and SKS arrivals recorded at 1056 stations to image the *S*-wave velocity structure of the Andean Subduction Zone beneath South America (Fig. 1c). Data used in the study is compiled from 52 temporary and permanent seismic networks across South America over the last 30 yr [see Table S1; Institut De Physique Du Globe De Paris (IPGP), & Ecole Et Observatoire Des Sciences De La Terre De Strasbourg (EOST) 1982; Scripps Institution of Oceanography 1986; Albuquerque Seismological Laboratory (ASL)/USGS 1988, 1993; GEOFON Data Centre 1993; Silver *et al.* 1994; Zandt 1996; Beck *et al.* 2000; Asch *et al.* 2002; Russo 2004, 2007; GFZ German Research Centre For Geosciences & Institut Des Sciences De L'Univers-Centre National De La Recherche CNRS-INSU 2006; Beck & Zandt 2007; Sandvol & Brown 2007; Gilbert 2008; Cesca *et al.* 2009; Pritchard 2009; Beck *et al.* 2010; Roecker & Russo 2010; Wagner *et al.* 2010; Waite 2010; West & Christensen 2010; Observatório Nacional, Rio de Janeiro, RJ 2011; Vilotte & RESIF
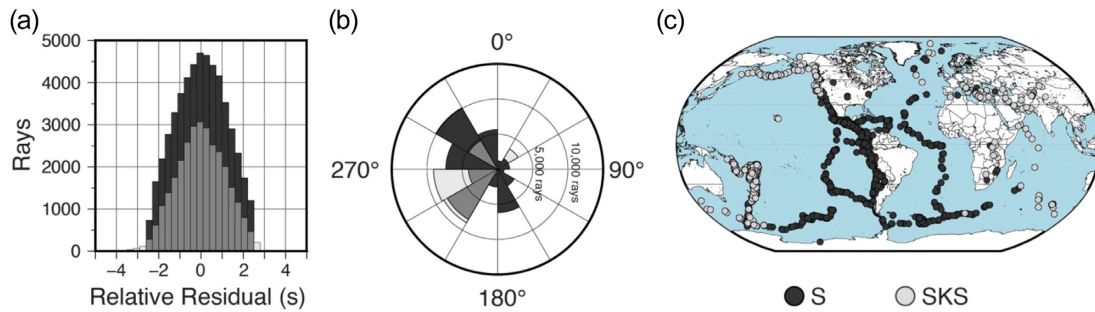
Figure 2. Data distribution. (a) Histogram of demeaned relative residuals for direct *S* (dark grey; *n* = 52 535) and SKS (transparent light grey; plotted on top of the *S* phases in plots a-b; *n* = 30 106) phases before inversion. (b) Backazimuth distribution of residuals divided into 30° bins. (c) Location of 1674 earthquakes ($M_w > 5$) used in our model (NEIC-USGS, USA Earthquake catalogue 2020).

2011; PeruSE 2013; Universidad de Chile 2013; Poveda *et al.* 2015; Meltzer & Beck 2016; Regnier *et al.* 2016; Ruiz 2016; Alvarado *et al.* 2018; Barrientos & National Seismological Center (CSN) Team 2018; Bianchi *et al.* 2018]. Our final data set includes 52 535 *S* and 30 106 SKS phase relative traveltime residuals from a combined data set of 1674 earthquakes of magnitude 5.0 and larger (Fig. 2). Traveltimes are determined using the multichannel cross-correlation technique of VanDecar & Crosson (1990), modified by Pavlis & Vernon (2010). Each waveform pick is visually inspected to remove falsely correlated phases (e.g. cycle-skipped phases). Direct *S* arrivals were picked on the transverse component of seismograms from epicentral distance of 30° to 90° and SKS arrivals on the radial component from epicentral distance of 100–120°. Traveltimes for both *S* and SKS phases are picked in three filtered frequency bands: 0.1–0.7 Hz (16 per cent of our final data set), 0.04–0.16 Hz (37 per cent) and 0.01–0.09 Hz (47 per cent) following prior teleseismic tomography models (Schmandt & Humphreys 2010; Scire *et al.* 2016).

2.2 Traveltime corrections

Relative traveltime measurements at each station are adjusted to account for the effect of local variations in crustal thickness by removing the estimated traveltime difference between the IASP91 crustal thickness of 35 km (Kennett & Engdahl 1991) and the estimated local crustal thickness. Local crustal thickness estimates are derived from a combination of receiver function, seismic reflection and gravity studies (Fig. S1; Assumpção *et al.* 2002, 2004, 2013; Niu *et al.* 2007; Julià *et al.* 2008; Lloyd *et al.* 2010; Tassara & Echaurren 2012; Poveda *et al.* 2015; Albuquerque *et al.* 2017; Condori *et al.* 2017; Rodriguez & Russo 2020). Where local data are not available, crustal thickness is estimated by interpolating nearby measurements. Traveltime residuals recorded at stations in the fore-arc are additionally adjusted to account for relatively faster lower crustal velocities, as is broadly seen in previous local and regional studies of the forearc (Graeber & Asch 1999; Koulakov *et al.* 2006; Schurr *et al.* 2006; Ward *et al.* 2013; Lynner *et al.* 2018, 2020).

Finally, SKS traveltimes are adjusted to account for azimuthal anisotropy by:

$$t_{\text{isotropic}} = t_{\text{ measured}} - \delta t \sin^2\phi \qquad (1)$$

(Stein & Wysession 2009; Nelson & Grand 2018), where t_{measured} is the traveltime of an SKS phase to a station, δt is the station-averaged delay time of the SKS arrival and ϕ is the angle between the station-averaged fast polarization angle and event backazimuth. Station averaged delay times are derived from a compilation of shear wave splitting studies (Silver & Chan 1991; Vinnik *et al.* 1992; Helffrich *et al.* 1994, 2002; Russo & Silver 1994; James & Assumpção 1996; Russo *et al.* 1996; Barruol & Hoffman 1999; Murdie & Russo 1999; Polet *et al.* 2000; Krüger *et al.* 2002; Heintz *et al.* 2003; Behn *et al.* 2004; Assumpção *et al.* 2006, 2011; Pinero-Feliciangeli & Kendall 2008; Growdon *et al.* 2009; Abt *et al.* 2010; Masy *et al.* 2011; Hicks *et al.* 2012; Nowacki *et al.* 2012, 2015; Rosa & Fuck 2012; Meighan & Pulliam 2013; Porritt *et al.* 2014; Wölbern *et al.* 2014; Bastow *et al.* 2015; Eakin *et al.* 2015, 2016, 2018; Idárraga-García *et al.* 2016; Long *et al.* 2016; Chagas de Melo *et al.* 2018; Reiss *et al.* 2018; Lynner & Beck 2020).

For stations without published shear wave splitting measurements, values from the nearest neighbouring station are used. If the nearest station is more than 50 km away, it is used only when it is within a similar tectonic province (e.g. if a station was located on a craton and the nearest station was not, the preferred splitting measurement substitute was taken from the closest station on the same craton). We show the effects of these corrections to our data set and model in Figs S2 and S3. Although the fit to the relative residuals did not improve significantly, the corrections resulted in non-negligible changes to the model (in some cases by >±4 per cent d*Vs*), the corrections overall do not affect our interpretations which rely more heavily on relative variations in structure. The most significant changes occur in the central part of the continent where SKS splitting is stronger and more regionally consistent over several hundreds of kilometres.

2.3 Tomographic inversion

We use the finite-frequency teleseismic tomography method of Schmandt & Humphreys (2010) to invert for *S*-wave velocity structure. This method initially traces rays using the 1-D IASP91 *S*-wave velocity model of Kennett & Engdahl (1991). Velocity sensitivities for each ray are then estimated using Born theoretical kernels within the first Fresnel Zone to approximate ray sampling (Dahlen *et al.* 2000; Schmandt & Humphreys 2010). The inversion uses damping, smoothing, and station and event terms to add constraints to the model (Schmandt & Humphreys 2010). Analysis of the trade-off between data variance reduction and the model norm is performed to choose damping and smoothing parameters of 4 and 5, respectively, for the final inversion (Fig. S4). This choice of parameters results in a variance reduction of 70 per cent for our final model.

We adopt the model space parametrization of SAM5_P_2019 (Portner *et al.* 2020), which divides the mantle into depth and distance dilating nodes. This node setup additionally accounts for the non-uniform station spacing across South America (Figs 1c and 3),
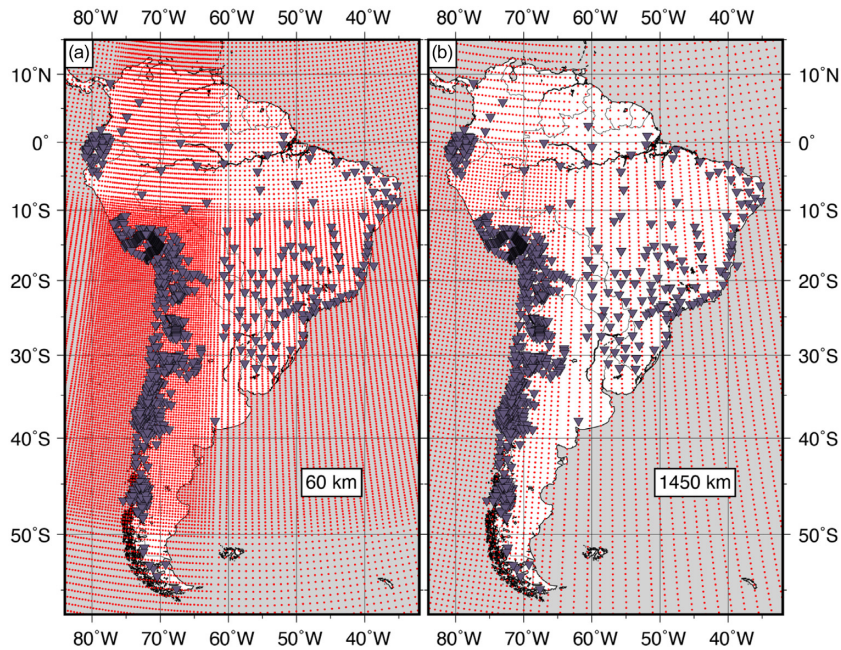
Figure 3. Model node distribution maps. Circles denote model node centres and inverted triangles show the locations of seismic stations, for reference. (a) The top layer of our model, 60 km depth. (b) The bottom-most layer of our model, 1450 km depth.

most notably in northern Perú, western Brazil, and Argentina, by placing the smallest nodes (35 km lateral spacing) beneath the Central Andes and increases spacing outward to 115 km where station density is lowest (Fig. 3). The full model-space extends from 60 to 1450 km depth, with the vertical thickness of nodes expanding from 35 km at the top of our model to 70 km in the lowermost layer. We additionally include a version of our model with double the lateral model spacing (70–230 km) in Figs S5 and S6. We note that the large-scale geometries and locations interpreted structures does not change in this model, but simply appear 'smoother'. The amplitudes of the anomalies decrease as expected with a smoother model (Figs S5 and S6).

After an initial *S*-wave tomography inversion using the 1-D ray tracing, the resulting velocity model is converted to absolute velocities using the ak135 *S*-wave velocity model (Kennett *et al.* 1995) through which rays are retraced in the upper 750 km using the FM-TOMO 3-D ray tracing code (de Kool *et al.* 2006; Rawlinson *et al.* 2006). This conversion to absolute velocities is used solely for the purpose of ray tracing and does not affect the velocity perturbations inverted for in the model. We then re-invert using the new ray paths. This process is repeated through six iterations following the initial inversion, resulting in a final velocity model using iterative 3-D ray tracing. The effects of 3-D ray tracing on our final model are shown in Fig. S7.

To characterize the sampling of data in our model space, we calculate normalized hit-quality (Fig. S8), following Schmandt & Humphreys (2010). Hit-quality ranges from 0 to 1, where 0 indicates that no rays sampled a given node and 1 indicates the node was 'perfectly' sampled. This measure weights the source location for rays by binning the rays of each bin into six groups by backazimuth as a proxy for crossing rays in each bin. A 'perfectly' sampled node therefore indicates that the node is sampled by a high number of rays from diverse backazimuths. For this study, we have chosen a hit-quality threshold of 0.4 to qualitatively represent adequate sampling based on the results of our synthetic resolution tests (see Section 3.1). We ignore regions in our model that have normalized hit quality <0.4.

3 RESOLUTION TESTS

As a means of assessing the robustness of our data and model, we rely on a suite of synthetic resolution tests and bootstrap resampling.

3.1 Bootstrapping analysis

We use bootstrapping to determine the standard deviation of each node of our model as shown in supplemental Figs S9 and S10. For the bootstrap resampling method, we randomly sample a subset of our data, with replacement, and rerun the tomographic inversion using the new data subset. This process is repeated 100 times, each with new, randomly selected data subsets, in order to fully characterize the stability of our result from our data set (Fig. S9). The effects of removed or duplicated rays are seen in the resulting model from each run. We then calculated the standard deviation of the resulting velocity models at each node in the model space over the 100 bootstrap runs (Fig. S9). This allows us to determine which anomalies within the model space are more confidently required by the data. For all bootstrap resampling and synthetic resolution tests we use the same model parameters as in our final model inversion (e.g. smoothing and damping) and refer to all results in terms of model perturbations, however due to the computational requirements of the 3-D ray tracing, the following resolution tests were calculated using the initial *S*-wave velocity model produced by the 1-D ray tracing.

The bootstrap results show that the standard deviations for most of the model space with denser station coverage beneath the high Andes is <1 per cent d*Vs*, compared to low elevation areas of Brazil and parts of eastern Argentina where the standard deviation reaches ~2 per cent d*Vs* due to the larger station spacing. Standard deviations exceed 3 per cent d*Vs* within the uppermost (60 and 95 km) and lowermost (1380 and 1450 km) layers of our model (Fig. S10), hence we do not interpret these layers in our model. Relatively high standard deviations are expected in these layers, since they have the fewest crossing rays and are where the inversion

typically places anomalies from outside of the model space (Schmandt & Humphreys 2010). We also observe a gradual increase in the average standard deviation with depth (Fig. S10). This correlates well with increases in amplitudes of the velocity perturbations with depth, excluding the aforementioned uppermost layers, indicating that the increase in variance is not a consequence of reduced stability with depth. Our final tomography model velocity perturbations generally varies within ± 8 per cent dVs with a few regions having perturbations as much as ± 15 per cent dVs. Hence, the anomalies we interpret are >2 per cent dVs (Fig. S8).

3.2 Checkerboard and recovery tests

To assess the resolution of recovered mantle structures in our tomography model we perform a number of synthetic tests (Figs 4 and 5). The first of these is a synthetic checkerboard test with input anomalies alternating $+9$ per cent dVs and -9 per cent dVs for every three nodes of our model separated by two nodes of 0 per cent dVs (Fig. 4). We note that the size of these input anomalies varies with that of the nodes, both laterally and with depth (Fig. 3). Checkerboard tests in cross-sectional views and of additional sizes are included in Figs S11–13. We do not include noise in our checkerboard or recovery tests.

The checkerboard tests reveal that the highest amplitudes recovered from our input anomalies occur beneath the Andean Cordillera and eastern Brazil at depths greater than 660 km (Figs 4d–f). We recover greater than half of our input anomalies across the model at these depths, with the exceptions of regions of Ecuador/northern Perú and southern Chile/Argentina. Overall, for these depths, we observe increased lateral smearing particularly in the westernmost portion of our model and decreased vertical smearing relative to the upper mantle. This result is somewhat expected because of the shallowing of ray incidence angle with depth. South of ~40°S we recover more of the input anomaly in the lower mantle (>660 km depth) than in the upper mantle and mantle transition zone layers. However, the recovered anomaly remains less than 50 per cent of the input anomaly across all depths at these latitudes. This reduction in recovered amplitudes likely corresponds to the decrease in station coverage to the south, with notably very few stations east of the Cordillera south of ~35°S.

In the upper mantle, the checkerboard test reveals high lateral resolution of our input anomaly and significant vertical smearing in most of the model beneath the Andean Cordillera and eastern Brazil (Figs 4a and b). The amplitudes recovered in these regions are considerably lower than at greater depths, recovering 15–20 per cent of our input anomaly on average. At these depths within the upper mantle, the consequence of uneven station density is most apparent. Beneath westernmost Brazil and Bolivia, east of the Andean Cordillera, we recover less than half of the input anomalies where station spacing can exceed 400 km. We additionally observe lateral smearing of the checkerboard anomalies, most notably in northeastern Brazil, near the Perú-Brazil border, and in southern Chile and Argentina. Throughout our model, we recover almost none of our input anomaly outside of the 0.4 hit-quality measure (Fig. 4). We therefore distinguish regions with the 0.4 hit-quality or higher as adequately sampled.

In addition to the traditional 'checkerboard' analysis, we performed a number of recovery tests simulating synthetic structures based on the anomalies that we observe, or would expect to observe, in our model. The first of these tests is a synthetic Nazca slab anomaly derived from the slab model of Portner *et al.* (2020), which is based on teleseismic *P*-wave tomography and earthquake data. The synthetic anomaly has an input anomaly of $+9$ per cent dVs. Recovery of the slab is qualitatively similar to that of the checkerboard test, with the highest recovered amplitudes (>50 per cent) at lower mantle depths (Fig. 5). Recovery of the input slab anomaly within the upper mantle is relatively poor in the northern region of our model space, beneath Perú and western Brazil. The recovered slab anomaly is more diffuse, with less than half of the input amplitude recovered (Fig. 5a). Further south, we recover similar amplitudes in the upper mantle, <50 per cent of the input anomaly, however there is significantly less lateral and vertical smearing of the slab anomaly with the highest recovered amplitudes at the centre of our input anomaly (Figs 5b–d).

Overall, our velocity model is well resolved from ~130 to 1200 km depth in the region of our >0.4 normalized hit quality contour. The results of our synthetic tests show that the amplitude and spatial resolution of our input anomalies is best recovered where station density is highest, beneath the Cordillera from 15°S to 40°S and eastern Brazil for the upper mantle. In the lower mantle, we see improved input anomaly recovery throughout, with the highest amplitudes recovered beneath Brazil, where node sizes are largest.

4 RESULTS

Our final *S*-wave tomography model, called SAM5_S_2020, using 3-D ray tracing is shown in Figs 6–8 and S14. Regions within our model that fall below the 0.4 hit-quality measure are greyed out and will not be discussed. We do not show regions in our model shallower than 130 km and deeper than 1200 km. The results of the bootstrap analyses and synthetic recovery tests show regions outside of these depths to be the least robust. Within these bounds, the maximum velocity perturbation is 13.2 per cent dVs, while typical velocity perturbations range from ± 8 per cent dVs. We note that because we use relative travel time arrivals as our input data, 0 per cent dVs represents the regional average of the mantle in our model. Thus, perturbations reported are regional deviations and are not tied to the global average and cannot be interpreted in terms of absolute velocity.

The most prominent feature in our model is a linear, high-amplitude, fast velocity anomaly (~7 per cent dVs), extending from ~5°N to 40°S and from the top of our model space (~130 km depth) to ~1100 km depth (Figs 6 and 7). This fast seismic velocity anomaly parallels the Perú–Chile trench and is coincident with previously interpreted Nazca slab seismicity and models of the Nazca slab itself (e.g. Cahill & Isacks 1992; Ammirati *et al.* 2016; Hayes *et al.* 2018; Portner *et al.* 2020). We therefore interpret this anomaly to be the Nazca slab. We note that the upper mantle image of the Nazca slab is somewhat limited by station distribution, manifesting as amplitude undulations within the slab anomaly (Fig. 6) as seen in our synthetic slab recovery tests (Fig. 5). This effect is diminished by ~240 km depth, where we recover a Nazca slab anomaly with more uniform velocity anomaly amplitudes (~7 per cent dVs; Figs 6 and 7).

The slab anomaly displays a general decrease in amplitude southward, from ~7 to 2 per cent dVs. This is likely a result of poorer resolution in the south as demonstrated by synthetic checkerboard and slab tests (Figs 4 and 5). The geometry of the slab anomaly also differs from north to south as it penetrates the lower mantle. Beneath Brazil, the Nazca slab thickens from ~200–300 km thick to >400 km thick as it enters the lower mantle and flattens
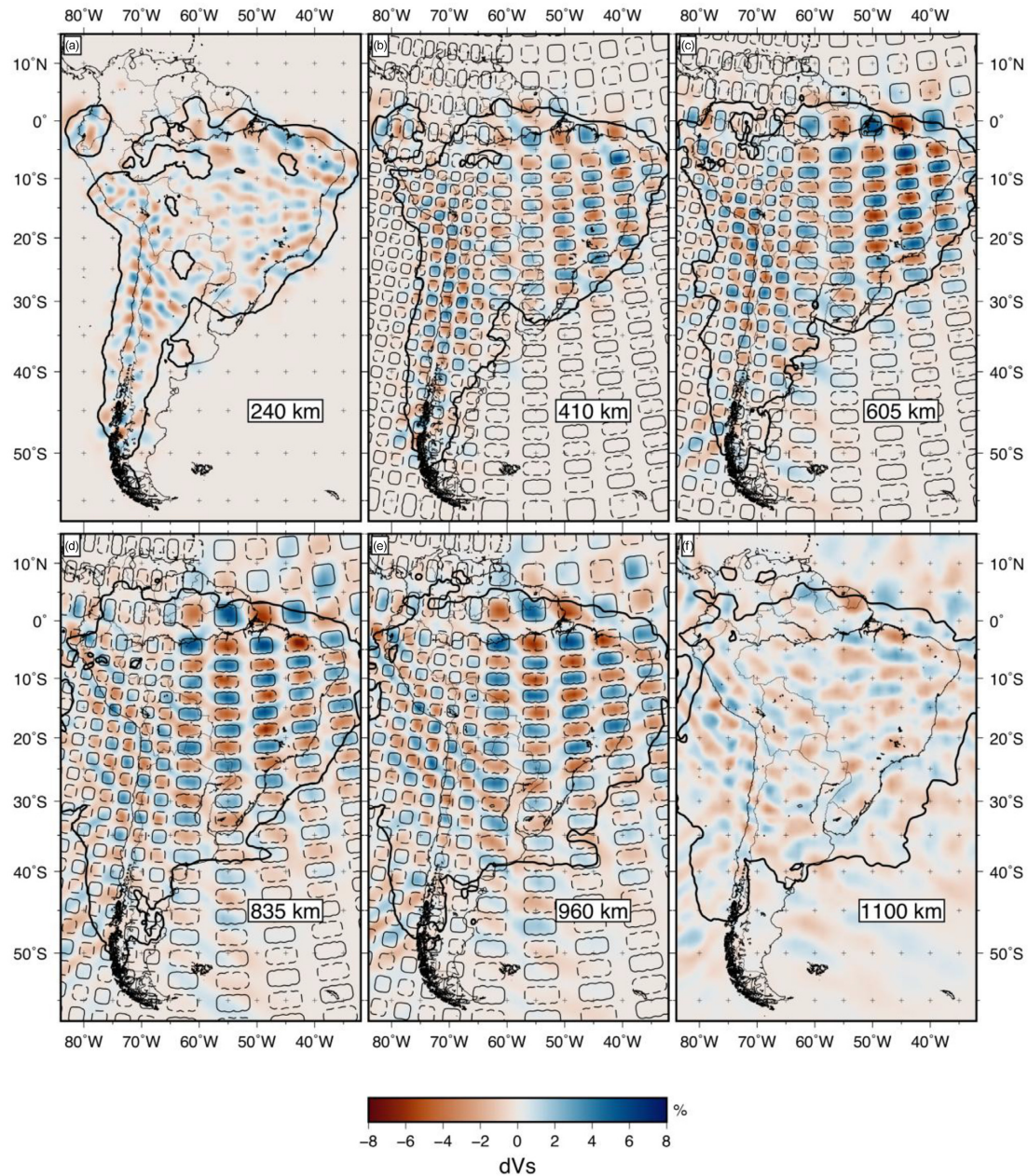
Figure 4. Synthetic checkerboard test for example depth slices. Depth slices for each map are denoted in the right corner. For all maps the black solid lines outline an input anomaly of +9 per cent d*Vs*. Dashed black lines outline an input anomaly of −9 per cent d*Vs*. Our input is designed as alternating positive and negative anomalies in 3 × 3 × 3 model nodes (Fig. 3) with alternating positive and negative anomalies separated by 2 model nodes with an input of 0 per cent d*Vs*. The recovered synthetic anomalies are shown by the coloured scale. Note (a) and (d) depth slices at 240 km and 1100 km do not have any input anomalies but we include them to show some vertical smearing. The thicker black line indicates the 0.4 hit-quality contour. Additional cross-sections and checkerboards of varying sizes are included in Figs S9–11.

at ~1000 km depth (Figs 7a, 7b and 8e). In contrast, beneath Argentina we see a Nazca slab that maintains a uniform thickness, ~200 km, and subduction angle as it goes from the upper mantle to the lower mantle (Fig. 7d). Continuity of the Nazca slab anomaly is disrupted beneath the Perú-Bolivia border (15–18°S) and beneath the Sierras Pampeanas (31–33°S). In these two regions, the slab anomaly disappears for a ~250 km in the lower mantle transition zone (~550–660 km) and upper mantle (~240–365 km), respectively (Figs 6b, d and 7d), before reemerging at greater depths.

In addition to the Nazca slab anomaly, we observe several high-amplitude features in our model. The first is a vertically oriented

slow velocity anomaly (S1) (−6 per cent d*Vs*) beneath the Peruvian Flat Slab (Figs 6a–c and 8a). This anomaly extends from the base of the slab anomaly to the bottom of the mantle transition zone, dipping gently westward (Fig. 8a). The shallow portion of this anomaly appears to extend laterally beneath the trench, southward along the margin until ~30°S. Synthetic recovery tests of this feature comparing two possible depth ranges, the first from 165 to 240 km (Fig. 9a), and a second from 165 to 505 km (Fig. 9b), show that less than 10 per cent of the input amplitude is recovered by the former case. In contrast, the deeper extending input anomaly is recovered by at least 50 per cent at its centre. Therefore, the observed extent of
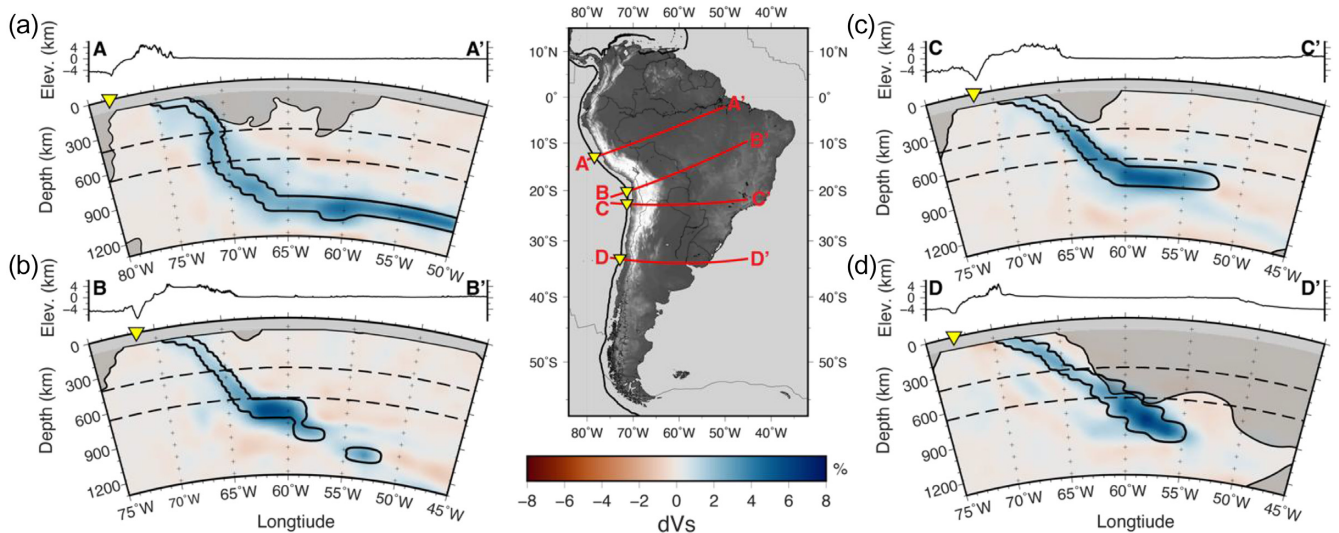
Figure 5. Synthetic slab anomalies test. For all cross-sections (a–d) the solid black line represents the 0.4 hit-quality contour. Greyed out are regions that scored a hit-quality of less than 0.4. The thicker black contour denotes the location of the synthetic input anomaly, the solid line shows the location of the +9 per cent d*Vs*. The recovered slab anomaly is shown by the coloured scale. The inverted triangle denotes the location of the trench on the inset map and corresponding cross-sections. Dashed lines correspond to depths of 410 and 660 km. Our input synthetic slab anomaly comes from the Nazca slab model of Portner *et al.* (2020).

the anomaly from 165 to 660 km depth is unlikely to be an artifact of smearing and is instead a robust result.

Further south directly beneath the slab, we image a relatively large fast velocity anomaly (F1) ranging from 200 km depth to the mantle transition zone that extends ∼1000 km along the South America margin (Figs 6a–d and 8b). This feature is subparallel to the slab in the mantle transition zone. Within the upper mantle, it appears somewhat amorphous with a more restricted along-margin extent beneath the region of the Sierras Pampeanas, between ∼25° and 35°S. This anomaly at most depths is similar in amplitude to the Nazca slab anomaly (∼7 per cent d*Vs*). Synthetic recovery tests of this fast velocity anomaly (F1) show that the top and bottom of this feature are well resolved, with very little vertical smearing in the lower mantle and high amplitude recovery at its centre (∼8 per cent d*Vs*, Fig. 9c), suggesting it is a real feature that we recover.

Beneath eastern Brazil, we observe a cylindrical, high-amplitude slow velocity anomaly (S2, Figs 7 and 8c–d). This anomaly appears as a relatively thin vertical feature at 130 km depth and subvertically extends to the bottom of our model. The anomaly is adjacent to the eastern edge of the Nazca slab anomaly where the slab flattens at ∼1000 km depth (Figs 8c–d). he northern edge of this slow anomaly connects with several other slow velocity anomalies in the lower mantle along the length of the Nazca slab beneath Brazil (Fig. 6f). Synthetic recovery tests of this vertical anomaly show that the anomaly is well resolved, with high amplitude recovery and very little vertical or lateral smearing (Fig. 9d), indicating that the geometry, depth and amplitude of perturbation of the anomaly observed are relatively robust.

5 DISCUSSION

5.1 The Nazca slab

The fast Nazca slab anomaly dominates our tomography model, extending from ∼5°S to 40°S in both the upper and lower mantle.

The imaged slab is coincident with Nazca Wadati-Benioff Zone earthquakes (Cahill & Isacks 1992) and displays a similar geometry as that imaged in previous *P*-wave velocity models (Pesicek *et al.* 2012; Bianchi *et al.* 2013; Scire *et al.* 2016, 2017; Portner *et al.* 2020). The slab anomaly within our model appears relatively thicker (∼200–300 km) than seen in that in SAM5_P_2019 (Portner *et al.* 2020) and other teleseismic *P*-wave models. This is expected because the *S* waves used in this study have broader sensitivity kernels, which naturally smooths the model relative to *P*-wave models.

With our model, we confirm that the slab anomaly continues into the lower mantle along the entire subduction zone, similar to Portner *et al.* (2020), with varying behavior and structure along strike. Beneath northern Brazil, the slab anomaly stagnates in the lower mantle around ∼1000–1100 km depth. Further south beneath Argentina, the slab appears to retain its subduction angle throughout the observable lower mantle. While the slab anomaly is not as clear south of 30° S due to sparser data coverage, we clearly do not observe the same large-scale slab stagnation at ∼1000–1100 km depth (Fig. 7d). Near 35°S–40°S, the slab anomaly extends offshore of Argentina and out of our area of resolution. If the slab does stagnate in the lower mantle in this region, it occurs east of the South America continent under the western Atlantic Ocean.

The stagnation of slabs within the lower mantle observed in other subduction zones around the globe (e.g. Fukao & Obayashi 2013; Goes *et al.* 2017) has been attributed to mantle layering caused by changes in composition and/or viscosity (Ballmer *et al.* 2015, 2017; Marquardt & Miyagi 2015; Goes *et al.* 2017) and/or slab properties such as strength (e.g. Billen & Hirth 2007; Li *et al.* 2015) or absolute motion (e.g. Billen 2010). For the Nazca slab, stagnation is unlikely to be related to variations in slab properties because the emergence of lower mantle stagnation does not match any known changes in slab properties, such as absolute motion and plate age. Motion is relatively uniform along the entire margin as well as relative plate convergence velocity during the past 10–20 Myr (Kendrick *et al.* 2003; DeMets *et al.* 2010), which promotes uniform stagnation across the margin. The age of the Nazca Plate decreases towards the south, making the southern, younger/weaker segment of the slab
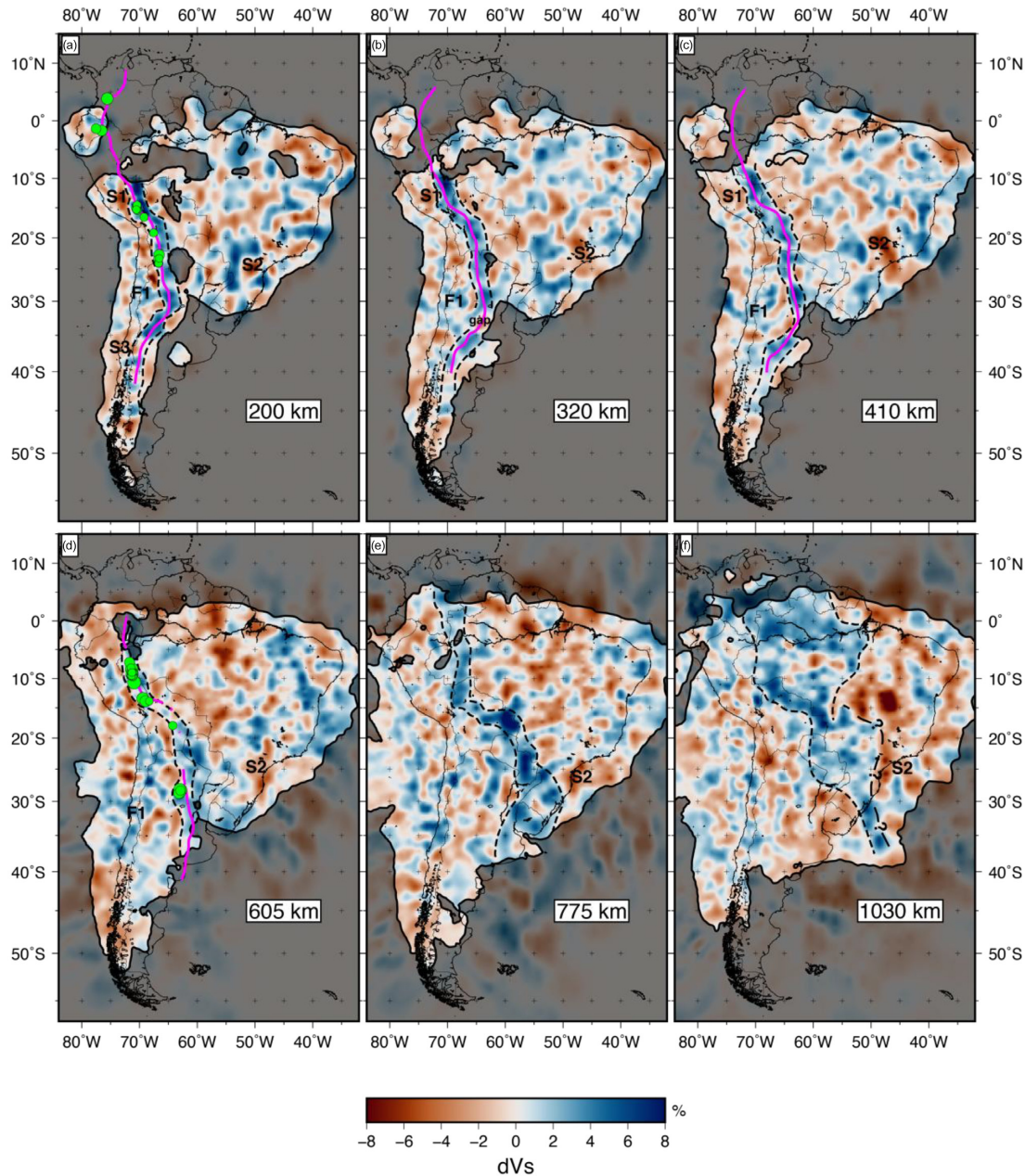
Figure 6. *S*-wave tomography model depth slices from the 3-D ray tracing results (SAM5_S_2020). For all layers the solid black line represents the 0.4 hit-quality contour. Greyed out are regions that scored a hit-quality of less than 0.4. The dashed line represents our interpreted Nazca slab anomaly. The Slab2 model of the Nazca slab at corresponding depths is denoted by the thicker contour (Hayes *et al.* 2018). The circles represent >*M* 5 earthquakes from 1960 to 1 January 2019 (NEIC-USGS, USA Earthquake catalogue 2020). F1: Fast velocity anomaly 1. S1–3: Slow velocity anomalies 1–3.

more likely to stagnate. Neither of these patterns matches what we presently observe.

The slab stagnation beneath Brazil at ∼1000–1100 km is more consistent with mantle layering hypotheses, which can vary over the observed length scales (Marquardt & Miyagi 2015). Ballmer *et al.* (2017) suggest there may be viscosity and compositional changes at ∼1000 km as a result of preserved bridgmanite-enriched lower mantle. These regions of bridgmanite-enriched mantle may be regionally preserved for long periods of time and separated by regions of upwellings due to mantle convection (Ballmer *et al.* 2017). If these or some other form of lower mantle viscosity layering (Marquardt & Miyagi 2015; Rudolph *et al.* 2015) exist, the regions

of slab stagnation at ∼1000–1100 km depth may give us clues to the scale of the mantle heterogeneity. In the case of the stagnant Nazca slab beneath Brazil it suggests that lower mantle viscosity jumps may expand over regions of at least 20° by 20°.

In the upper mantle, we observe two gaps within the Nazca slab anomaly. The first is located at ∼18°S at ∼550 km depth (Fig. 7a). This gap has been previously observed in an *S*-wave tomography model of the region (Scire *et al.* 2016) but is absent in *P*-wave tomography studies (Fig. S15; Scire *et al.* 2016, 2017; Portner *et al.* 2020). Synthetic recovery tests indicate that a gap of this size is difficult to resolve due to low amplitude recovery and significant smearing in this region (Figs 9a and S16). This suggests that
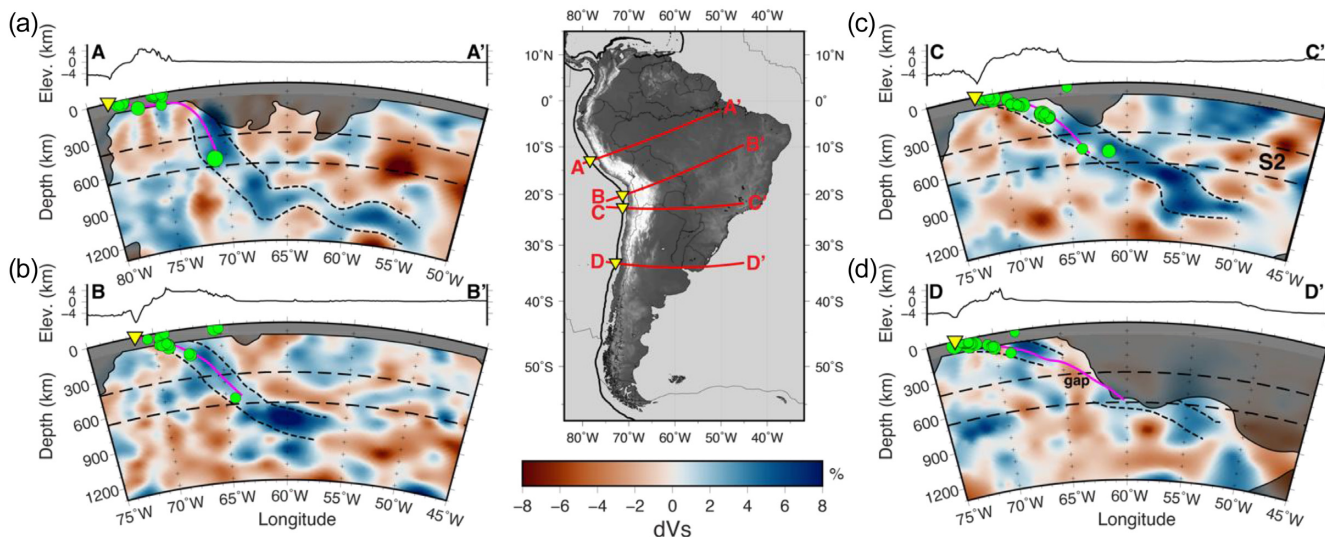
Figure 7. *S*-wave tomography model cross-sections from the 3-D ray tracing results. For all cross-sections (a–d) the solid black line represents the 0.4 hit-quality contour. Greyed out are regions that scored a hit-quality of less than 0.4. The dashed line represents our interpreted Nazca slab anomaly. The Slab2 model of the Nazca slab at corresponding depths is denoted by the thicker contour (Hayes *et al.* 2018). The circles represent >*M* 5 earthquakes from 1960 to 1 January 2019 (NEIC-USGS, USA Earthquake catalogue 2020). The inverted triangle denotes the location of the trench on the inset map and corresponding cross-sections. S2: Slow velocity anomaly 2.
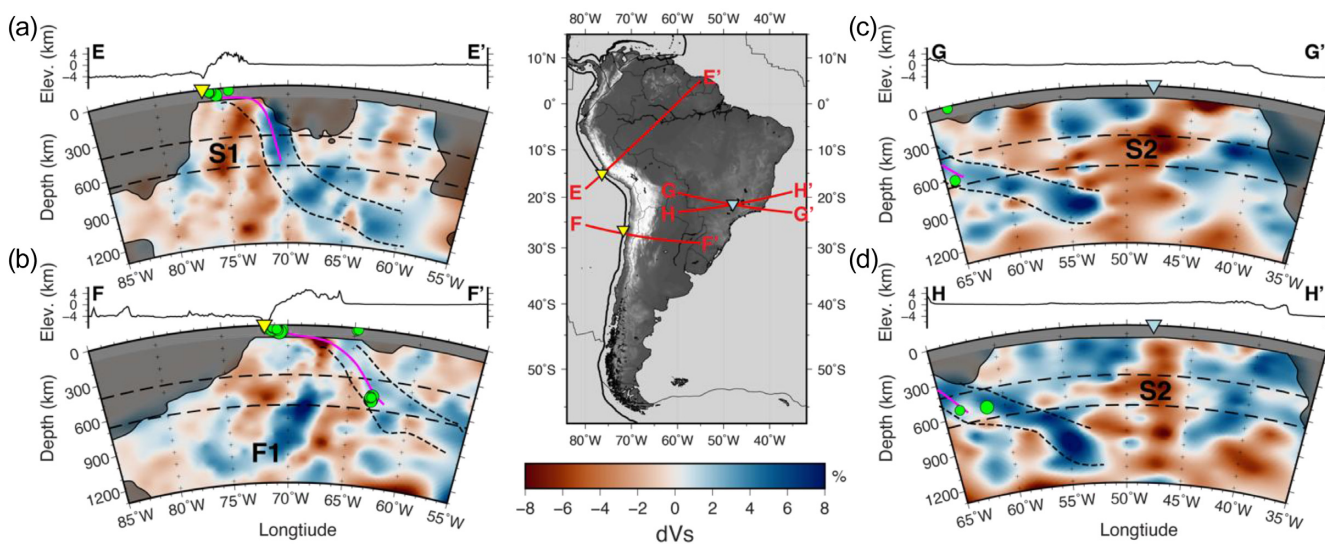

Figure 8. *S*-wave tomography model cross-sections from the 3-D ray tracing results. For all cross-sections (a–d) the solid black line represents the 0.4 hit-quality contour. Greyed out are regions that scored a hit-quality of less than 0.4. The dashed line represents our interpreted Nazca slab anomaly. The Slab2 model of the Nazca slab at corresponding depths is denoted by the thicker contour (Hayes *et al.* 2018). The circles represent >*M* 5 earthquakes from 1960 to 1 January 2019 (NEIC-USGS, USA Earthquake catalogue 2020). For cross-sections a–b, the inverted triangle denotes the location of the trench For cross-sections c–d, the inverted triangle represents an arbitrary reference point for the Paraná basin (see inset map). F1: Fast velocity anomaly 1. S1–2: Slow velocity anomalies 1–2.`

the imaged slab gap in our model near the Bolivia orocline is not sufficiently resolved to contradict prior suggestions of a continuous slab (Portner *et al.* 2020).

The second slab gap is observed beneath the eastern Sierras Pampeanas at the southern edge of the Pampean Flat Slab, extending from ∼200 to 400 km depth (Figs 6b and 7d). Within this gap we observe a relatively slow velocity anomaly (−3 per cent d*Vs*) that extends from the lower mantle through the slab gap. Synthetic resolution tests that include a similar feature suggest the gap is resolvable (Fig. S15). Additionally, a gap within the slab anomaly here

has been well imaged in previous teleseismic tomography studies (Fig. S16; Portner *et al.* 2017, 2020) and is supported by shear wave splitting observations (Lynner *et al.* 2017).

The slow velocities imaged within the gap appears to extend from the gap to at least 900 km depth and possibly to the base of the model (1200 km depth). In the lower mantle, the anomaly appears to spread out and/or connect with other low velocity material giving it the appearance of a plume-like feature (Fig. 7d). Given the structure and that slow velocities at these depths are most commonly attributed to hot temperatures, the anomaly is consistent with prior
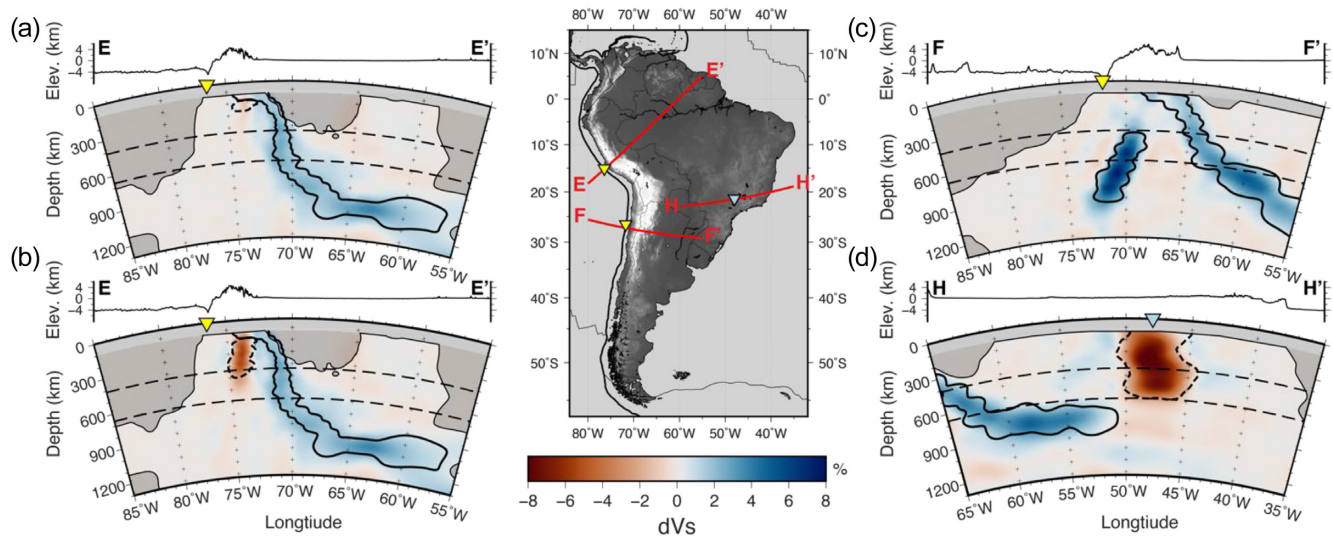
Figure 9. Synthetic slab and mantle anomalies test. For all cross-sections (a-d) the solid black line represents the 0.4 hit-quality contour. Greyed out are regions that scored a hit-quality of less than 0.4. The thicker black contour denotes the location of the synthetic input anomaly, the solid line shows the location of the +9 per cent d*Vs*. Dashed lines show the location of the −9 per cent d*Vs* input anomaly. The recovered anomalies are shown by the coloured scale. For cross-sections a–c, the inverted triangle denotes the location of the trench. For cross-sections c–d, the inverted triangle represents an arbitrary reference point for the Paraná basin (see inset map). Synthetic tests are shown for (a) a shallow S1 anomaly with a synthetic input extending from 165 to 240 km depth; (b) a deeper S1 anomaly with a synthetic input extending from 165 to 505 km depth; (c) the F1 anomaly extending from 410 to 895 km; (d) the S2 anomaly extending from 60 to 660 km depth.

interpretations of it being a conductive feature such as a plume (Burd *et al.* 2013). Portner *et al.* (2017), using a sub-set of the same stations and *P*-wave tomography, did not image the slow velocity anomaly extending into the lower mantle prompting them to hypothesize that the slow velocity material represents asthenospheric mantle being dragged into the subduction zone from an offshore hotspot. This inconsistency could be due to the differences in the capabilities of *P* and *S* waves to capture slow velocity anomalies, where *S* waves can potentially provide higher resolution images of slow velocity anomalies due to the stronger effects of slower velocities on delay times (e.g. Maguire *et al.* 2016, 2018). However, this requires further investigation for this region.

5.2 The surrounding mantle

We image several high amplitude seismic velocity anomalies within the mantle surrounding the Nazca slab including two slow velocity anomalies (S1 and S2, Fig. 8) and a high amplitude fast velocity anomaly (F1, Fig. 8) that we discuss below.

5.2.1 Subslab slow velocity anomalies

The most prominent slow velocity anomaly within the upper mantle near the slab lies beneath the Peruvian Flat Slab (anomaly S1) and extends from beneath the flat slab to the base of the mantle transition zone (∼660 km depth). The slow velocity anomaly beneath Perú has been imaged by a variety tomography studies (Amaru 2007; Li *et al.* 2008; Antonijevic *et al.* 2015, 2016; Scire *et al.* 2016, 2017; Portner *et al.* 2020). The nature of this anomaly has attracted several viable scenarios of its origin including: asthenospheric upwelling related to locally thinned oceanic mantle lithosphere associated with the Nazca Ridge (Scire *et al.* 2016), volatile-enriched submantle (Antonijevic *et al.* 2016), or hotspot material entrained by the motion of the Nazca slab (Portner *et al.* 2017). In our model, this anomaly

(∼−5 per cent slow) extends into the mantle transition zone (Fig. 8a) implying a deeper origin than these upper mantle related hypotheses. This observation is consistent with the SAM5_P_2019 teleseismic *P*-wave model (Portner *et al.* 2020) which shows the anomaly down to ∼900 km depth.

Regardless of its origin, the anomaly likely represents relatively hot, buoyant mantle. Its existence may impact the behavior of the Nazca slab by increasing the local buoyancy beneath the slab. The Peruvian flat slab flattens at a depth of 70 km (Bishop *et al.* 2017; Antonijevic *et al.* 2015) before resteepening into the mantle at a near vertical angle, ∼400–500 km from the trench (this study; Antonijevic *et al.* 2016; Scire *et al.* 2016, 2017; Portner *et al.* 2020). The flattening of the slab has been linked to the subduction of the over-thickened oceanic crust of the Nazca Ridge (Gutscher *et al.* 2000). Numerical models have suggested, however, that the increased buoyancy associated with overthickened oceanic crust may not be enough to flatten the slab on its own, calling for other mechanisms such as over-thrusting of the overriding plate (van Hunen *et al.* 2002), subslab overpressure (Schepers *et al.* 2017), or slab-suction (Manea *et al.* 2012) to contribute to slab flattening. Using receiver functions, Bishop *et al.* (2017) suggest the oceanic crust of the Nazca Plate is eclogitized ∼350 km from the trench, and that the slab should therefore be resteepening nearer to the trench than is observed if supported solely by slab buoyancy. Bishop *et al.* (2017) attribute the continued flattening of the slab to buoyancy forces associated with hot subslab mantle. Our model shows the slow anomaly extending to shallow depths (∼130–200 km) coincident with the inboard extension of the Peruvian flat slab, supporting the hypothesis that it represents a volume of buoyant sub-slab mantle material.

The additional buoyancy provided by hot subslab mantle may impact coupling along the subduction zone interface. We observe relatively shallow (<200 km depth) slow velocities along several other parts of the South America margin in addition to the prominent slow velocity anomaly beneath Perú. The most laterally continuous of these subslab slow velocity anomalies is between ∼34° and ∼45°

S (Fig. 10). This subslab slow is coincident with the 1960 M_w 9.5 Valdivia earthquake rupture and the 2010 M_w 8.8 Maule earthquake rupture (Barrientos & Ward 1990; Lay *et al.* 2010), suggesting a possible correlation between sub-slab slow velocities and increased megathrust plate coupling (Fig. 10). If these subslab slow velocity anomalies represent asthenospheric upwellings and hence, cause some small increased mantle buoyancy they may contribute to plate boundary segmentation. The increase mantle buoyancy could be one factor of many that could increase the plate coupling at the megathrust interface along the segment.

Other smaller subslab slow velocity anomalies are observed in northern Chile and southern Perú, but they are more limited in size and may not be sufficiently resolved in our model to correlate them with any one earthquake rupture. For example, a small, low-amplitude anomaly is coincident with the M_w 8.3 2015 Illapel earthquake rupture in central Chile (Melgar *et al.* 2016). However, there is evidence of several varying sized ruptures during different earthquake cycles along the coast of Chile near ∼34°S and 20°S (e.g. Ruiz & Madariaga 2018) that makes it difficult to assess its direct relationship to the observed slow velocities. More detailed seismic tomography along the trench is needed to improve resolution along the western South America margin to confirm the correlation between possible mantle upwelling and any particular plate boundary segmentation. Similarly, sub-slab slow velocity anomalies of a comparable size and extent have been imaged at other subduction zones, including Cascadia where subslab slow velocity anomalies beneath the trench correlate with possible megathrust rupture segments (Bodmer *et al.* 2018). Bodmer *et al.* (2018) suggested that the subslab buoyancy modulates the thrust interface coupling.

5.2.2 The Paraná plume anomaly

Beneath the Paraná Basin in easternmost Brazil is a second high-amplitude slow velocity anomaly (anomaly S2; Figs 8c and d). This anomaly has been imaged using both teleseismic *P*- and *S*-wave tomography and the vertical geometry of the anomaly has led to its designation as the 'Paraná plume' (VanDecar *et al.* 1995; Schimmel *et al.* 2003; Rocha *et al.* 2011). It is unclear from previous studies the extent of the plume in the upper and lower mantle leaving its origins enigmatic. Determining the origin of this anomaly has been hindered by a lack of surface expression related to a plume (e.g. high heat flow, recent volcanism, etc.). Previous interpretations of the anomaly have included a fossil conduit of the Tristan da Cunha hotspot (VanDecar *et al.* 1995), which currently resides beneath the Mid-Atlantic Ridge, and an upwelling produced by edge driven convection as the result of the disruption of mantle flow from a cratonic lithosphere root (King & Ritsema 2000; Assumpção *et al.* 2004, King 2007; Rocha *et al.* 2016, 2019a, b). The most recent volcanism in the region comes from flood basalts and alkali volcanism dated to between 80 and 137 Ma, corresponding to the opening of the South Atlantic Ocean and the impingement of the Tristan da Cunha plume (e.g. Thiede & Vasconcelos 2010). However, as pointed out by VanDecar *et al.* (1995) if the surface volcanic outcrops are related to the imaged mantle fossil plume then the entire upper mantle must have moved with the South America Plate over the last 80–137 Ma.

Our model shows the slow anomaly extending well into the lower mantle (at least to 1200 km) and is located directly adjacent to the southern edge of the stagnant Nazca slab at ∼1000–1100 km depth. The bottom of this anomaly is unresolved at the base of our model and may extend deeper than 1200 km. The position of the anomaly

does not agree with predictions made by the fossil plume hypothesis. The westward absolute motion of the South America Plate predicts the anomaly would be much further east if it were associated with the Tristan da Cunha plume rather than beneath the modern exposure of volcanic rocks. Additionally, anomaly S2 appears to connect with several slow velocity anomalies along the entire margin of the Nazca slab at ∼1000 km depth beneath Brazil (Fig. 6) suggesting the anomaly is sourced by a much broader feature.

We offer a new interpretation for the origin of the 'plume' based on its widespread lateral extent and its relationship with the Nazca slab. We propose that the Paraná 'plume' anomaly is the result of a localized upwelling induced by the continued motion of the leading edge of the stagnant Nazca slab (Fig. 11). Plume formation and focused 'wet' upwellings can occur as the result of a stagnant slab entering the lower mantle (e.g. Faccenna *et al.* 2010; Richard & Iwamori 2010). Similarly, the descent of slabs into the lower mantle can disrupt the thermal stability of the mantle at the tip of the slab, forming focused upwellings (Tan *et al.* 2002). The stagnation of the Nazca slab may be producing a similar effect, creating a 1000-km-thick convection cell and inducing a focused upwelling beneath the Paraná Basin. Both models match the distribution of slow velocity anomalies surrounding the Nazca slab in the lower mantle within our tomography model.

Alternatively, it is possible that the slab is stagnating in response to an existing plume rather than inducing the plume. This would appear similarly in our results. This hypothesis has been proposed for the Tonga slab, which stagnates within the mantle transition zone where it intersects the Somoan plume rising beneath it (Chang *et al.* 2016). We may be seeing a similar process beneath South America where Paraná plume induces stagnation of the Nazca slab at ∼1000 km depth. Such a model requires rapid trench retreat following stagnation (Chang *et al.* 2016). In our case, there is a lack of evidence for a recent pulse of rapid trench retreat of the South American margin, beyond the background westward migration of South America (e.g. Seton *et al.* 2012). Additionally, contact between the Paraná 'plume' and the Nazca slab occurs at one edge of the stagnated slab and not along the entire margin, with 'normal' subduction occurring to the south, making this scenario unlikely. We would also expect a thermal anomaly at the surface if this were a typical plume sourced at the core–mantle boundary.

From our tomography model alone, the nature of this upwelling is difficult to resolve. We are unable to determine whether the slow anomaly is a thermal perturbation (Tan *et al.* 2002), or 'wet' (Faccenna *et al.* 2010) from the tomography alone. There is no evidence for a large thermal perturbation at the surface, suggesting that this large slow velocity anomaly is not thermal in origin. Focused studies on the Paraná plume have proposed that the slow velocity anomaly is likely related to a localized compositional change (e.g. Liu *et al.* 2003; Rocha *et al.* 2011) lending support for its interpretation as a 'wet' plume. Additionally, receiver function studies of the upper mantle transition zone in the Paraná Basin (Liu *et al.* 2003; Bianchi *et al.* 2019) have not detected any anomaly that could be attributed to a thermal origin. However, most numerical models and imaging studies that suggest the formation of 'wet' plumes focus on slab stagnation or fragmentation in the mantle transition zone rather than the lower mantle (e.g. Faccenna *et al.* 2010; Tao *et al.* 2018). Recent studies suggest that there are hydrous mineral phases in slabs that are stable at pressure and temperature conditions in the lower mantle that could contribute to a seismic low velocity anomaly (Schmandt *et al.* 2014; Ohtani 2015; Hermann & Mookherjee 2016). While it is unclear if a slab can retain enough hydrous mineral phases to produce a 'wet' upwelling in the lower mantle, the lack of a
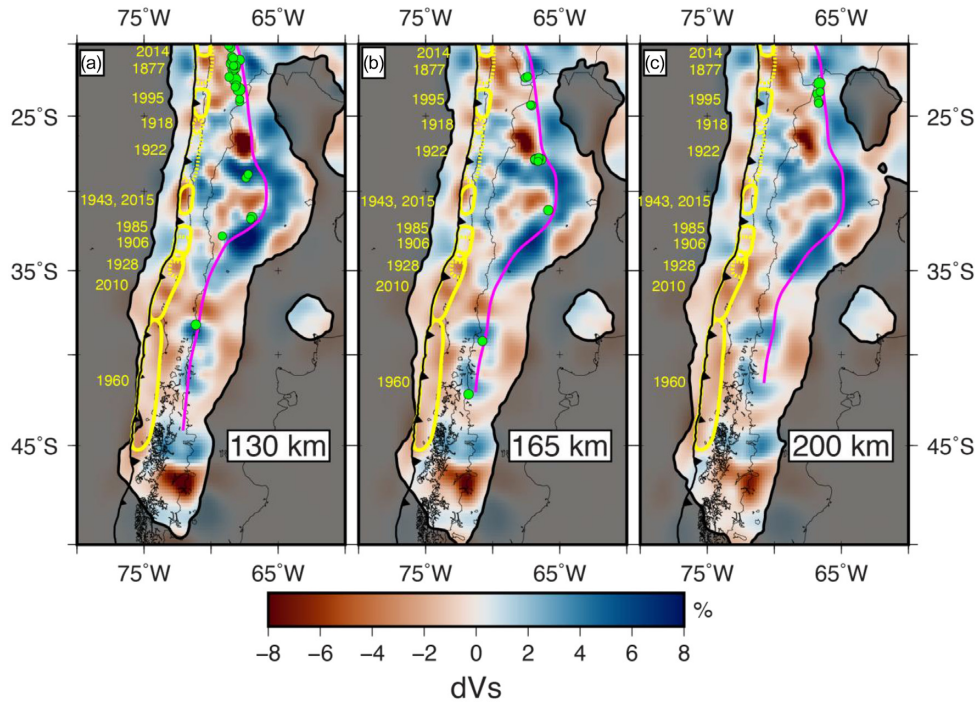
Figure 10. SAM5_S_2020 focused on Chile and Argentina. Outlined are the estimated rupture regions for the largest megathrust earthquakes denoted by years (Barrientos & Ward 1990; Lay *et al.* 2010; Melgar *et al.* 2016). Dashed lines represent less certain ruptures. The Slab2 model of the Nazca slab at corresponding depths is denoted by the thicker contour (Hayes *et al.* 2018). The circles represent >*M* 5 earthquakes from 1960 to 1 January 2019 (NEIC-USGS, USA Earthquake catalogue 2020).
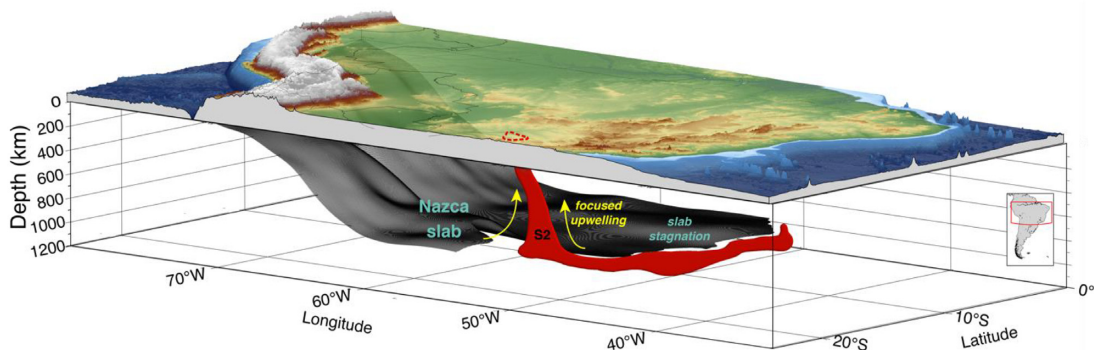

Figure 11. Cartoon interpretation of the S2 anomaly beneath the Paraná basin. The S2 slow velocity anomaly's interpreted geometry is represented by the eastern-most surface. The western-most surface shows the top of the Nazca slab anomaly from our *S*-wave tomography model. The dashed line plotted on the topography shows the location of the S2 anomaly from the 130 km depth slice.

measured heat flow anomaly or recent volcanic rocks at the surface suggests the upwelling maybe related to hydration and compositional changes. Our *S*-wave images of this deep-rooted low velocity zone is consistent with upwelling of material leaving open the possibility that the Nazca slab retained sufficient hydrous phases into the lower mantle to excite a 'wet' plume.

5.2.3 A relic slab in the mantle?

In addition to the slow velocity anomalies in the mantle, a high-amplitude fast velocity anomaly (anomaly F1, Fig. 8b) lies beneath the Chile trench adjacent to the Pampean Flat Slab. This fast anomaly occurs between ∼25°S and 35°S and extends variably from ∼200 km depth at some latitudes to ∼1000 km depth at others. Within the mantle transition zone, the anomaly appears parallel to

the Nazca slab anomaly. The amplitude of this anomaly (∼+4–5 per cent), particularly in the mantle transition zone, is similar to, and at some depths higher than, the Nazca slab anomaly (Fig. 8b). This anomaly has been imaged in previous teleseismic *P* wave (Pesicek *et al.* 2012; Portner *et al.* 2017, 2020; Scire *et al.* 2017) and global imaging studies (e.g. Li *et al.* 2008), but with variable shape, size, and amplitude.

The shallow depth of the top of the F1 anomaly (∼200–400 km) may suggest that it is a relatively young feature. Slab sinking rates are extremely variable but assuming a globally averaged slab sinking rate of ∼1–2 cm yr^{-1} (e.g. Butterworth *et al.* 2014), this feature could be as young as 10–20 Ma. It is unlikely to be a part of the Nazca slab as the slab anomaly is continuous into the lower mantle, extending for >2000 km in length directly adjacent to the F1 anomaly (this study, Portner *et al.* 2020). With no obvious recent evidence of tear

in the Nazca slab that would give rise to the size of the F1 anomaly, it needs to be much older than the Nazca slab. Additionally, the Nazca–South America trench has experienced >900 km of westward trench retreat over the last ∼50 Ma (e.g. O'Neill *et al.* 2005; Torsvik *et al.* 2008; Doubrovine *et al.* 2012; Somoza & Ghidella 2012; Schepers *et al.* 2017), thus any broken off remnant segment of the Nazca slab would be expected much further east.

If the F1 anomaly is indeed older than Nazca subduction, then it may be a relic slab that has become trapped in the upper mantle and is not sinking at typical rates, despite being beneath an actively subducting plate. Plate reconstructions of the southeastern Pacific have proposed the existence of an oceanic spreading ridge, between the Farallon and Phoenix (or Aluk) plates, which subducted beneath South America during the Palaeogene (e.g. Cande & Leslie 1986; Somoza & Ghidella 2012; Maloney *et al.* 2013; Gianni *et al.* 2018, Fig. S17). Maloney *et al.* (2013) further divide the Phoenix Plate into two smaller plates, the Chasca and Catequil plates but for our purposes we will refer to it as the Phoenix Plate. The exact location and evolution of the Farallon-Phoenix ridge subduction at the trench is uncertain, but estimates suggest that it may have subducted initially near 30°S–36°S relative to the present trench (Aragón *et al.* 2013; Maloney *et al.* 2013; Gianni *et al.* 2018) and then migrated southward. The Phoenix Plate was completely subducted by Late Cretaceous (Maloney *et al.* 2013; Gianni *et al.* 2018). The subduction of this oceanic ridge (between the Phoenix and Farallon plates) has been coupled with a proposed detachment of the Phoenix Plate in most plate reconstructions (Somoza & Ghidella 2012; Aragón *et al.* 2013; Gianni *et al.* 2018). The F1 anomaly could be a remnant of the Phoenix slab which detached and stagnated in the mantle transition zone prior to the Nazca slab subduction in this region. Becoming stagnant is possible with an extremely young slab and/or if the slab were to become entrapped by a small-scale convection cell (e.g. Simmons *et al.* 2015; Wang *et al.* 2018). This model, however, still fails to reconcile the westward retreat of the South America margin where we would continue to expect an old slab fragment to be further southeast of the present-day trench. Further work on plate reconstructions and mantle flow are needed to determine if our suggestion that the F1 anomaly is a slab relic.

Another possibility is that the F1 anomaly may not be a relic slab but instead may be a compositional anomaly relative to the surrounding mantle. It has been proposed by Ballmer *et al.* (2017) that compositional layering of the lower mantle at ∼1000 km depth could prevent full-mantle convection. Disruption of full-mantle convection could produce long-lived dense materials which resist mantle entrainment of convections cells and are perhaps seismically detectable (Ballmer *et al.* 2017). Although compositional layering is possible, the elongate shape of the anomaly and the high amplitude (∼5 per cent) of the anomaly lead us to prefer a slab origin for the F1 anomaly.

6 CONCLUSIONS

We present a 3-D ray tracing finite-frequency teleseismic S-wave tomography model (SAM5_S_2020) for the mantle above 1200 km depth beneath South America. Our model reveals a continuous Nazca slab subducting eastward beneath South America from the top of our model to ∼1100 km depth which is consistent with previous imaging studies (e.g. Portner *et al.* 2020). Lower mantle penetration by the slab is characterized by a discrete change in slab morphology along strike, from a high-amplitude slab anomaly which broadens and flattens or stagnates at ∼1000 km beneath

Brazil to a less coherent, weakened slab anomaly which appears to subduct at a ∼30° dip through the transition zone beneath Argentina. The stagnation of the Nazca slab at 1000 km depth beneath Brazil is potentially coupled with a focused upwelling at the southern edge of the flattened slab, beneath the Paraná Basin of Brazil. We suggest this low velocity anomaly may be related to slab dehydration in the lower mantle.

We image several extensive slow velocity anomalies beneath the Nazca slab which may, in part, locally increase mantle buoyancy beneath the slab. We image a slow-velocity anomaly which extends from the mantle transition zone to ∼165–200 km depth beneath the inboard extension of the Peruvian Flat Slab. Its buoyancy likely contributes to prolonged flattening of the slab.

We also see a fast, slab-like anomaly beneath the Nazca slab in the region of central Chile, extending variably ∼200–1000 km depth, which we suggest could be a relic slab segment, possibly related to the Phoenix/Aluk Plate which subducted along the margin during the Palaeogene. However, further work on plate reconstructions and mantle flow are needed to determine how such a slab could persist in the upper mantle with current understandings of reconstructions of the Nazca–South America subduction zone.

REFERENCES

Abt, D.L., Fischer, K.M., Abers, G.A., Protti, M., Gonzalez, V. & Strauch, W., 2010. Constraints on upper mantle anisotropy surrounding the Cocos slab from SK(K)S splitting, *J. geophys. Res.,* **115,** B06316, doi:10.1029/2009jb006710.

Albuquerque, D.F., Franca, G.S., Moreira, L.P., Assumpção, M., Bianchi, M., Barros, L.V., Quispe, C.C. & Oliveira, M.E., 2017. Crustal structure of the Amazonian Craton and adjacent provinces in Brazil, *J. South Am. Earth Sci.,* **79,** 431–442.

Albuquerque Seismological Laboratory (ASL)/USGS, 1988. *Global Seismograph Network (GSN - IRIS/USGS).* International Federation of Digital Seismograph Networks. Other/Seismic Network. https://doi.org/10.7914/SN/IU.

Albuquerque Seismological Laboratory (ASL)/USGS, 1993. *Global Telemetered Seismograph Network (USAF/USGS).* International Federation of Digital Seismograph Networks. Other/Seismic Network. https://doi.org/10.7914/SN/GT.

& Alvarado, A., Ruiz, M., Mothes, P., Yepes, H., Segovia, M., Vaca, M. & Aguilar, J., ..., 2018. Seismic, volcanic, and geodetic networks in

Ecuador: building capacity for monitoring and research, *Seismol. Res. Lett.,* **89**(2A), 432–439.

Amaru, M.L., 2007. *Global Travel Time Tomography with 3-D Reference Models,* Vol. 274, Utrecht University.

Ammirati, J-B., Pérez Luján, S., Alvarado, P., Beck, S., Rocher, S. & Zandt, G., 2016. High-resolution images above the Pampean flat slab of Argentina (31–32° S) from local receiver functions: Implications on regional tectonics, *Earth planet. Sci. Lett.,* **450**(15), 29–39.

Antonijevic, S.K., Wagner, L.S., Beck, S.L., Long, M.D., Zandt, G. & Tavera, H., 2016. Effects of change in slab geometry on the mantle flow and slab fabric in Southern Peru, *J. geophys. Res.,* **121**(10), 7252–7270.

Antonijevic, S.K., Wagner, L.S., Kumar, A., Beck, S.L., Long, M.D., Zandt, G., Tavera, H. & Condori, C., 2015. The role of ridges in the formation and longevity of flat slabs, *Nature,* **524**(7564), 212–215.

Aragón, E. *et al.*, 2013. The Farallon-Aluk ridge collision with South America: implications for the geochemical changes of slab window magmas from fore-to back-arc, *Geoscience Frontiers,* **4**(4), 377–388.

Asch, G., Heit, B. & Yuan, X., 2002. *The ReFuCA project: Receiver Functions Central Andes*. Deutsches GeoForschungsZentrum GFZ. https://doi.org/10.14470/mn7557778612.

Assumpção, M., An, M., Bianchi, M., França, G.S., Rocha, M., Barbosa, J.R. & Berrocal, J., 2004. Seismic studies of the Brasília fold belt at the western border of the São Francisco Craton, Central Brazil, using receiver function, surface-wave dispersion and teleseismic tomography, *Tectonophysics,* **388**(1–4), 173–185.

Assumpção, M., Guarido, M., van der Lee, S. & Dourado, J.C., 2011. Upper-mantle seismic anisotropy from SKS splitting in the South American stable platform: a test of asthenospheric flow models beneath the lithosphere, *Lithos.,* **3**(2), 173–180.

Assumpção, M., Heintz, M., Vauchez, A. & Egydio Silva, M., 2006. Upper mantle anisotropy in SE and Central Brazil from SKS splitting: evidence of asthenospheric flow around a cratonic keel, *Earth planet. Sci. Lett.,* **250**, 224–240.

Assumpção, M., James, D. & Snoke, A., 2002. Crustal thicknesses in SE Brazilian Shield by receiver function analysis: implications for isostatic compensation, *J. geophy. Res.,* **107**(B1), doi:10.1029/2001JB000422.

Assumpção, M. *et al.*, 2013. Crustal thickness map of Brazil: data compilation and main features, *J. South Am. Earth Sci.,* **43**, 74–85.

Ballmer, M.D., Houser, C., Hernlund, J.W., Wentzcovitch, R.M. & Hirose, K., 2017. Persistence of strong silica-enriched domains in the Earth's lower mantle, *Nat. Geosci.,* **10**(3), 236.

Ballmer, M.D., Schmerr, N.C., Nakagawa, T. & Ritsema, J., 2015. Compositional mantle layering revealed by slab stagnation at∼ 1000-km depth, *Sci. Adv.,* **1**(11), e1500815.

Barrientos, S.E. & Ward, S.N., 1990. The 1960 Chile earthquake: inversion for slip distribution from surface deformation, *Geophys. J. Int.,* **103**(3), 589–598.

Barrientos, S. National Seismological Center (CSN) Team, 2018. The seismic network of Chile, *Seismol. Res. Lett.,* **89**(2A), 467–474.

Barruol, G. & Hoffman, R., 1999. Upper mantle anisotropy beneath the Geoscope stations, *J. geophys. Res.,* **104**(B5), 10757–10773.

Bastow, I.D., Julia, J., do Nascimzento, A.F., Fuck, R.A., Buckthorp, T.L. & McClellan, J.J., 2015. Upper mantle anisotropy of the Borborema Province, NE Brazil: implications for intra-plate deformation and sub-cratonic asthenospheric flow, *Tectonophys.*, **657**, 81–93.

Beck, S.L., Wallace, T. & Zandt, G., 2000. *Slab Geometry in the Southern Andes*. International Federation of Digital Seismograph Networks. Other/Seismic Network. https://doi.org/10.7914/SN/YC_2000.

Beck, S.L. & Zandt, G., 2007. *Lithospheric Structure and Deformation of the Flat Slab Region of Argentina*. International Federation of Digital Seismograph Networks. Other/Seismic Network. https://doi.org/10.7914/SN/ZL_2007.

Beck, S.L., Zandt, G. & Wagner, S., 2010. *Central Andean Uplift and the Geodynamics of the High Topography*. International Federation of Digital Seismograph Networks. **Other/Seismic Network**. https://doi.org/10.7914/SN/ZG_2010.

Behn, M.D., Conrad, C.P. & Silver, P.G., 2004. Detection of upper mantle flow associated with the African Superplume, *Earth planet. Sci. Lett.,* **224,** 259–274.

Bianchi, M., Assumpção, M., Koch, C. & Beck, S.L., 2019. Effect of the cold Nazca slab on the depth of the 660 km discontinuity in South America, in *Proceedings of the8th Int'l Symposium on Andean Geodynamics,* Sept. 2019, Quito, Ecuador.

Bianchi, M.B. *et al.*, 2018. The Brazilian seismographic network (RSBR): improving seismic monitoring in Brazil, *Seis. Res. Lett.,* **89**(2A), 452–457.

Bianchi, M. *et al.*, 2013. Teleseismic tomography of the southern Puna plateau in Argentina and adjacent regions, *Tectonophysics,* **586,** 65–83.

Bijwaard, H., Spakman, W. & Engdahl, E.R., 1998. Closing the gap between regional and global travel time tomography, *J. geophys. Res.,* **103**(B12), 30 055–30 078.

Billen, M.I., 2010. Slab dynamics in the transition zone, *Phys. Earth planet. Inter.,* **183**(1–2), 296–308.

Billen, M.I. & Hirth, G., 2007. Rheologic controls on slab dynamics, *Geochem. Geophys. Geosyst.,* **8**(8), doi:10.1029/2007GC001597.

Bishop, B, Beck , S L, Zandt, G, Wagner, L, Long, M, Antonijevic, S K, Kumar, A & Tavera, H., 2017. Causes and consequences of flat-slab subduction in southern Peru *Geosphere,* 13(5), 1392–1407, 10.1130/GES01440.1.

Bodmer, M., Toomey, D.R., Hooft, E.E. & Schmandt, B., 2018. Buoyant asthenosphere beneath Cascadia influences megathrust segmentation, *J. geophys. Res.,* **45**(14), 6954–6962.

Burd, A.I., Booker, J.R., Mackie, R., Pomposiello, C. & Favetto, A., 2013. Electrical conductivity of the Pampean shallow subduction region of Argentina near 33° S: Evidence for a slab window, *Geochem. Geophys. Geosyst.,* **14**(8), 3192–3209.

Butterworth, N.P., Talsma, A.S., Müller, R.D., Seton, M., Bunge, H.P., Schuberth, B.S.A., Shephard, G.E. & Heine, C., 2014. Geological, tomographic, kinematic and geodynamic constraints on the dynamics of sinking slabs, *J. Geodyn.,* **73,** 1–13.

Cahill, T. & Isacks, B.L., 1992. Seismicity and shape of the subducted Nazca plate, *J. geophys. Res.,* **97**(B12), 17 503–17 529.

Cande, S.C. & Leslie, R.B., 1986. Late Cenozoic tectonics of the southern Chile trench, *J. geophys. Res.,* **91**(B1), 471–496.

Celli, N.L., Lebedev, S., Schaeffer, A.J., Ravenna, M. & Gaina, C., 2020. The upper mantle beneath the South Atlantic Ocean, South America and Africa from waveform tomography with massive data sets, *Geophys. J. Int.,* **221**(1), 178–204.

Cesca, S., Sobiesiak, M., Tassara, A., Olcay, M., Günther, E., Mikulla, S. & Dahm, T., 2009. *The Iquique Local Network and PicArray*. GFZ Data Services. Other/Seismic Network. https://doi.org/10.14470/VD070092.

Chagas de Melo, B. & Assumpcção, M. 3-Basins Project Team, 2018. Mantle anisotropy and asthenospheric flow around cratons in southeastern South America, *Geophys. J. Int.,* **215**, 494–506.

Chang, S.J., Ferreira, A.M. & Faccenda, M., 2016. Upper-and mid-mantle interaction between the Samoan plume and the Tonga–Kermadec slabs, *Nature Comm.,* **7,** 10799.

Coffin, M.F., Gahagan, L.M. & Lawler, L.A., 1998. *Present-day Plate Boundary Digital Data Compilation*. University of Texas Institute for Geophysics Technical Report No. 174, 5.

Condori, C., França, G.S., Tavera, H.J., Albuquerque, D.F., Bishop, B.T. & Beck, S.L., 2017. Crustal structure of north Peru from analysis of teleseismic receiver functions, *J. South Am. Earth Sci.,* **76,** 11–24.

Dahlen, F.A., Hung, S.H. & Nolet, G., 2000. Fréchet kernels for finite-frequency traveltimes—I. Theory, *Geophys. J. Int.,* **141**(1), 157–174.

de Kool, M., Rawlinson, N. & Sambridge, M., 2006. A practical grid-based method for tracking multiple refraction and reflection phases in three-dimensional heterogeneous media, *Geophys. J. Int.,* **167**(1), 253–270.

DeMets, C., Gordon, R.G. & Argus, D.F., 2010. Geologically current plate motions, *Geophys. J. Int.,* **181**(1), 1–80.

Doubrovine, P.V., Steinberger, B. & Torsvik, T.H., 2012. Absolute plate motions in a reference frame defined by moving hot spots in the Pacific, Atlantic, and Indian oceans, *J. geophys. Res.,* **117**(B9), doi:10.1029/2011JB009072.

Eakin, C.M., Long, M.D., Scire, A., Beck, S.L., Wagner, L.S., Zandt, G. & Tavera, H., 2016. Internal deformation of the subducted Nazca slab inferred from seismic anisotropy, *Nat. Geosci.,* **9**(1), 56.

Eakin, C.M., Long, M.D., Wagner, L.S., Beck, S.L. & Tavera, H., 2015. Upper mantle anisotropy beneath Peru from SKS splitting: Constraints on flat slab dynamics and interaction with the Nazca Ridge, *Earth planet. Sci. Lett.,* **412,** 152–162.

Eakin, C.M., Rychert, C.A. & Harmon, N., 2018. The role of oceanic transform faults in seafloor spreading: a global perspective from seismic anisotropy, *J. geophys. Res.,* **123,** 1736–1751.

Faccenna, C., Becker, T.W., Jolivet, L. & Keskin, M., 2013. Mantle convection in the Middle East: reconciling Afar upwelling, Arabia indentation and Aegean trench rollback, *Earth planet. Sci. Lett.,* **375,** 254–269.

Faccenna, C., Becker, T.W., Lallemand, S., Lagabrielle, Y., Funiciello, F. & Piromallo, C., 2010. Subduction-triggered magmatic pulses: a new class of plumes?, *Earth planet. Sci. Lett.,* **299**(1–2), 54–68.

Fukao, Y. & Obayashi, M., 2013. Subducted slabs stagnant above, penetrating through, and trapped below the 660 km discontinuity, *J. geophys. Res.,* **118**(11), 5920–5938.

GEOFON Data Centre., 1993. *GEOFON Seismic Network*. Deutsches Geo-ForschungsZentrum GFZ. https://doi.org/10.14470/tr560404.

GFZ German Research Centre For Geosciences, & Institut Des Sciences De L'Univers-Centre National De La Recherche CNRS-INSU., 2006. *IPOC Seismic Network*. Integrated Plate boundary Observatory Chile - IPOC. https://doi.org/10.14470/pk615318.

Gianni, G.M., Pesce, A. & Soler, S.R., 2018. Transient plate contraction between two simultaneous slab windows: insights from Paleogene tectonics of the Patagonian Andes, *J. Geodyn.,* **121,** 64–75.

Gilbert, H., 2008. *Lithospheric Structure Above the Variably Dipping Nazca Slab*. International Federation of Digital Seismograph Networks. Other/Seismic Network. https://doi.org/10.7914/SN/XH_2008.

Goes, S., Agrusta, R., Van Hunen, J. & Garel, F., 2017. Subduction-transition zone interaction: a review, *Geosphere,* **13**(3), 644–664.

Graeber, F.M. & Asch, G., 1999. Three-dimensional models of P wave velocity and P-to-S velocity ratio in the southern central Andes by simultaneous inversion of local earthquake data, *J. geophys. Res.,* **104**(B9), 20 237–2056.

Growdon, M.A., Pavlis, G.L., Niu, F., Vernon, F.L. & Rendon, H., 2009. Constraints on mantle flow at the Caribbean - South American plate boundary inferred from shear wave splitting, *J. geophys. Res.,* **114,** doi:10.1029/2008JB005887.

Gutscher, M.-A., Spakman, W., Bijwaard, H. & Engdahl, E.R., 2000. Geodynamics of flat subduction: seismicity and tomographic constraints from the Andean margin, *Tectonics,* **19**(5), 814–833.

Hayes, G.P., Moore, G.L., Portner, D.E., Hearne, M., Flamme, H., Furtney, M. & Smoczyk, G.M., 2018. Slab2, a comprehensive subduction zone geometry model, *Science,* **362**(6410), 58–61.

Heintz, M., Vauchez, A., Assumpção, M., Barruol, G. & Egydio-Silva, M., 2003. Shear wave splitting in SE Brazil: an effect of active or fossil upper mantle flow, or both?, *Earth planet. Sci. Lett.,* **211,** 79–95.

Helffrich, G., Silver, P.G. & Given, H., 1994, Shear wave splitting variations over short spatial scales on continents, *Geophys. J. Int.,* **119,** 561–573.

Helffrich, G., Wiens, D.A., Vera, E., Barrientos, S., Shore, P., Robertson, S. & Adaros, R., 2002. A teleseismic shear-wave splitting study to investigate mantle flow around South America and implications for plate-driving forces, *Geophys. J. Int.,* **149,** F1–F7.

Hermann, A. & Mookherjee, M., 2016. High-pressure phase of brucite stable at Earth's mantle transition zone and lower mantle conditions, *Proc. Natl. Acad. Sci.,* **113**(49), 13971–13976.

Hicks, S.P., Nippress, Stuart E.J. & Rietbrock, A., 2012. Sub-slab mantle anisotropy beneath south-central Chile, *Earth planet. Sci. Lett.,* **357–358,** 203–213.

Horton, B.K., 2018. Tectonic regimes of the central and southern Andes: responses to variations in plate coupling during subduction, *Tectonics,* **37**(2), 402–429.

Hu, J., Liu, L., Faccenda, M., Zhou, Q., Fischer, K.M., Marshak, S. & Lundstrom, C., 2018. Modification of the Western Gondwana craton by plume–lithosphere interaction, *Nat. Geosci.,* **11**(3), 203–210.

Idárraga-García, J., Kendall, J.M. & Vargas, C.A., 2016. Shear wave anisotropy in northwestern South America and its link to the Caribbean and Nazca subduction geodynamics, *Geochem. Geophys. Geosyst.,* **17,** 1–19.

Institut De Physique Du Globe De Paris (IPGP), & Ecole Et Observatoire Des Sciences De La Terre De Strasbourg (EOST), 1982. *GEOSCOPE, French Global Network of Broad Band Seismic Stations*. Institut de Physique du Globe de Paris (IPGP). https://doi.org/10.18715/geoscope.g.

James, D.E. & Assumpção, M., 1996. Tectonic implications of S-wave anisotropy beneath SE Brazil, *Geophys. J. Int.,* **126,** doi:10.1111/j.1365-246X.1996.tb05263.x.

Julià, J., Assumpção, M. & Rocha, M.P., 2008. Deep crustal structure of the Parana Basin from receiver functions and Rayleigh-wave dispersion: evidence for a fragmented cratonic root, *J. geophys. Res.,* **113**(B8), doi:10.1029/2007JB005374.

Kendrick, E., Bevis, M., Smalley, R., Jr, Brooks, B., Barriga, R., Lauría, E. & Souto Fortes, L.P., 2003. The Nazca–South America Euler vector and its rate of change, *J. S. Am. Earth Sci.,* **16**(2) 125–131.

Kennett, B.L. & Engdahl, E.R., 1991. Traveltimes for global earthquake location and phase identification, *Geophys. J. Int.,* **105**(2), 429–465.

Kennett, B.L., Engdahl, E.R. & Buland, R., 1995. Constraints on seismic velocities in the Earth from traveltimes, *Geophys. J. Int.,* **122**(1), 108–124.

King, S.D., 2007. Hotspots and edge-driven convection, *Geology,* **35**(3), 223–226.

King, S.D. & Ritsema, J., 2000. African hot spot volcanism: small-scale convection in the upper mantle beneath cratons, *Science,* **290**(5494), 1137–1140.

Koulakov, I., Sobolev, S.V. & Asch, G., 2006. P- and S-velocity images of the lithosphere-asthenosphere system in the Central Andes from local-source tomographic inversion, *Geophys. J. Int.,* **167**(1), 106–126.

Krüger, F., Scherbaum, F., Rosa, J.W.C., Kind, R., Zetsche, F. & Höhne, J., 2002. Crustal and upper mantle structure in the Amazon region (Brazil) determined with broadband mobile station, *J. geophys. Res.,* **107,** doi:10.1029/2001JB000598.

Lay, T., Ammon, C.J., Kanamori, H., Koper, K.D., Sufri, O. & Hutko, A.R., 2010. Teleseismic inversion for rupture process of the 27 February 2010 Chile (Mw 8.8) earthquake, *J. geophys. Res.,* **37**(13), doi:10.1029/2010GL043379.

Li, C., Van Der Hilst, R.D., Engdahl, E.R. & Burdick, S., 2008. A new global model for P wave speed variations in Earth's mantle, *Geochem. Geophys. Geosyst.,* **9**(5), doi:10.1029/2002JB002208.

Liu, K.H., Gao, S.S., Silver, P.G. & Zhang, Y., 2003. Mantle layering across central South America, *J. geophys. Res.,* **108**(B11), doi:10.1029/2002JB002208.

Li, Y.Q., Ma, C.Q., Robinson, P.T., Zhou, Q. & Liu, M.L., 2015. Recycling of oceanic crust from a stagnant slab in the mantle transition zone: evidence from Cenozoic continental basalts in Zhejiang Province, SE China, *Lithos,* **230,** 146–165.

Lloyd, S., Van Der Lee, S., França, G.S., Assumpção, M. & Feng, M., 2010. Moho map of South America from receiver functions and surface waves, *J. geophys. Res.,* **115**(B11), doi:10.1029/2009JB006829.

Long, M.D., Biryol, C.B., Eakin, C.M., Beck, S.L., Wagner, L.S., Zandt, G., Minaya, E. & Tavera, H., 2016. Overriding plate, mantle wedge, slab, and subslab contributions to seismic anisotropy beneath the northern Central Andean Plateau, *Geochem. Geophys. Geosyst.,* **17,** 2556–2575.

Lu, C., Grand, S.P., Lai, H. & Garnero, E.J., 2019. TX2019slab: a new P and S tomography model incorporating subducting slabs, *J. geophys. Res.,* **124**(11), 11 549–11 567.

Lynner, C., Anderson, M.L., Portner, D.E., Beck, S.L. & Gilbert, H., 2017. Mantle flow through a tear in the Nazca slab inferred from shear wave slitting, *Geophys. Res. Lett.,* **44,** doi:10.1002/ 2017GL074312.

Lynner, C. & Beck, S.L., 2020. Subduction dynamics and structural controls on shear wave splitting along the South American convergent margin, *J. S. Am. Earth Sci,* **104,** 102824.

Lynner, C., Beck, S.L., Zandt, G., Porritt, R.W., Lin, F-.C. & Eilon, Z., 2018. Midcrustal deformation in the Central Andes constrained by radial anisotropy, *J. geophys. Res.,* **123**(6), 4798–4813, .

Lynner, C. *et al.*, 2020. Upper-plate structure in Ecuador coincident with the subduction of the Carnegie Ridge and the southern extent of large mega-thrust earthquakes, *Geophys. J. Int.,* **220**(3), 1965–1977.

Maguire, R., Ritsema, J., Bonnin, M., van Keken, P.E. & Goes, S., 2018. Evaluating the resolution of deep mantle plumes in teleseismic traveltime tomography, *J. geophys. Res.,* **123**(1), 384–400.

Maguire, R., Ritsema, J., van Keken, P.E., Fichtner, A. & Goes, S., 2016. P-and S-wave delays caused by thermal plumes, *Geophys. J. Int.,* **206**(2), 1169–1178.

Maloney, K.T., Clarke, G.L., Klepeis, K.A. & Quevedo, L., 2013. The Late Jurassic to present evolution of the Andean margin: drivers and the geological record, *Tectonics,* **32**(5), 1049–1065.

Manea, V.C., Pérez-Gussinyé, M. & Manea, M., 2012. Chilean flat slab subduction controlled by overriding plate thickness and trench rollback, *Geology,* **40**(1), 35–38.

Marquardt, H. & Miyagi, L., 2015. Slab stagnation in the shallow lower mantle linked to an increase in mantle viscosity, *Nat. Geosci.,* **8**(4), 311.

Masy, J., Niu, F., Levander, A. & Schmitz, M., 2011. Mantle flow beneath northwestern Venezuela: seismic evidence for a deep origin of the Mérida Andes, *Earth planet. Sci. Lett.,* **305**, 396–404.

Meighan, H.E. & Pulliam, J., 2013. Seismic anisotropy beneath the Northeastern Caribbean: implications for the subducting North American lithosphere, *Bull. Soc. Geol. Fr.,* **184**, 67–76.

Melgar, D. *et al.*, 2016. Slip segmentation and slow rupture to the trench during the 2015, Mw8. 3 Illapel, Chile earthquake, *J. geophys. Res.,* **43**(3), 961–966.

Meltzer, A. & Beck, S.L., 2016. *2016 Pedernales Earthquake Aftershock Deployment Ecuador*. International Federation of Digital Seismograph Networks. Other/Seismic Network. https://doi.org/10.7914/SN/8G_2016.

Murdie, R.E. & Russo, R.M., 1999. Seismic anisotropy in the region of the Chile margin triple junction, *J. S. Am. Earth Sci.,* **12**, 261–270.

Mégard, F., 1987. Cordilleran Andes and Marginal Andes: a Review of Andean Geology North of the Arica Elbow 18° S. *Circum-Pacific Orogenic Belts and Evolution of the Pacific Ocean Basin,* **18**, 71–95.

NEIC Earthquake catalogue, 2020. National Earthquake Information Centre, On-line Bulletin, http://earthquake.usgs.gov/earthquakes/search/.

Nelson, P.L. & Grand, S.P., 2018. Lower-mantle plume beneath the Yellowstone hotspot revealed by core waves, *Nat. Geosci.,* **11**(4), 280.

Niu, F., Bravo, T., Pavlis, G., Vernon, F., Rendon, H., Bezada, M. & Levander, A., 2007. Receiver function study of the crustal structure of the southeastern Caribbean plate boundary and Venezuela, *J. geophys. Res.,* **112**(B11), doi:10.1029/2006JB004802.

Nowacki, A., Kendall, J.M. & Wookey, J., 2012. Mantle anisotropy beneath the Earth's mid-ocean ridges, *Earth planet. Sci. Lett.,* **317–318**, 56–67.

Nowacki, A., Kendall, J.M., Wookey, J. & Pemberton, A., 2015. Mid-mantle anisotropy in subduction zones and deep water transport, *Geochem. Geophys. Geosyst.,* **16**, 764–784.

O'Neill, C., Müller, D. & Steinberger, B., 2005. On the uncertainties in hot spot reconstructions and the significance of moving hot spot reference frames, *Geochem. Geophys. Geosyst.,* **6**(4), doi:10.1029/2004GC000784.

Observatório Nacional, Rio de Janeiro, R.J., 2011. *Rede Sismográfica do Sul e do Sudeste (RSIS)*. International Federation of Digital Seismograph Networks. Other/Seismic Network. https://doi.org/10.7914/SN/ON.

Ohtani, E., 2015. Hydrous minerals and the storage of water in the deep mantle, *Chem. Geology,* **418**, 6–15.

Pavlis, G. & Vernon, F., 2010. Array processing of teleseismic body waves with the USArray, *Comput. Geosci.,* **36**, 910–920.

PeruSE, 2013. *Peru Subduction Experiment*. Caltech. Dataset. https://doi.org/10.7909/C3H41PBZ.

Pesicek, J.D., Engdahl, E.R., Thurber, C.H., DeShon, H.R. & Lange, D., 2012. Mantle subducting slab structure in the region of the 2010 M 8.8 Maule earthquake (30–40 S), Chile, *Geophys. J. Int.,* **191**(1), 317–324.

Pinero-Feliciangeli, L.T. & Kendall, J.M., 2008. Sub-slab mantle flow parallel to the Caribbean plate boundaries: Inferences from SKS splitting, *Tectonophys,* **462**, 22–34.

Polet, J., Silver, P.G., Beck, S., Wallace, T., Zandt, G., Ruppert, S., Kind, R. & Rudloff, A., 2000. Shear wave anisotropy beneath the Andes from the BANJO, SEDA, and PISCO experiments, *J. geophys. Res.,* **105**(B3), 6287–6304.

Porritt, R.W., Becker, T.W. & Monsalve, G., 2014. Seismic anisotropy and slab dynamics from SKS splitting recorded in Colombia, *Geophys. Res. Lett.,* **41,** doi:10.1002/2014GL061958.

Portner, D.E., Beck, S., Zandt, G. & Scire, A., 2017. The nature of subslab slow velocity anomalies beneath South America, *Geophys. Res. Lett.,* **44**(10), 4747–4755.

Portner, D.E. *et al.*, 2020. Detailed structure of the subducted Nazca slab into the lower mantle derived from continent-scale teleseismic P-wave tomography, *J. geophys. Res.,* e53955.

Poveda, E., Monsalve, G. & Vargas, C.A., 2015. Receiver functions and crustal structure of the northwestern Andean region, Colombia, *J. geophys. Res.,* **120**(4), 2408–2425.

Pritchard, M., 2009. *The Life Cycle of Andean Volcanoes: Combining Space-Based and Field Studies*. International Federation of Digital Seismograph Networks. Other/Seismic Network. https://doi.org/10.7914/SN/YS_2009.

Rapela, C.W. & Baldo, E.G, 2014. El cratón del Río de la Plata en la provincia de Córdoba, in *Relatorio del XIX Congreso Geológico Argentino, Córdoba, Argentina, 2014,* pp. 871–880.

Rawlinson, N., de Kool, M. & Sambridge, M., 2006. Seismic wavefront tracking in 3D heterogeneous media: applications with multiple data classes, *Explor. Geophys.,* **37**(4), 322–330.

Regnier, M., Font, Y., Charvis, P., Mercerat, D., Rietbrock, A., Ruiz, M. & Alvarado, A., 2016. *Pedernales*. International Federation of Digital Seismograph Networks. Other/Seismic Network. https://doi.org/10.7914/SN/XE_2016.

Reiss, M.C., Rümpker, G. & Wölbern, I., 2018. Large-scale trench-normal mantle flow beneath central South America, *Earth planet. Sci. Lett.,* **482**, 115–125.

Richard, G.C. & Iwamori, H., 2010. Stagnant slab, wet plumes and Cenozoic volcanism in East Asia, *Phys. Earth planet. Sci. Int.,* **183**(1–2), 280–287.

Rocha, M.P., Assumpção, M., Affonso, G.M.P.C., de Azevedo, P.A. & Bianchi, M., 2019b, Teleseismic P-wave Tomography Beneath the Pantanal, Paraná and Chaco-Paraná Basins, SE South America: delimiting Lithospheric Blocks of the SW Gondwana Assemblage, *J. geophys. Res.,* **124**, 2018JB016807.

Rocha, M.P., Azevedo, P.A., Marotta, G.S., Schimmel, M. & Fuck, R., 2016. Causes of intraplate seismicity in central Brazil from travel time seismic tomography, *Tectonophysics,* **680**, 1–7.

Rocha, M.P., de Azevedo, P.A., Assumpção, M., Pedrosa-Soares, A.C., Fuck, R. & Von Huelsen, M.G., 2019a, Delimiting the Neoproterozoic São Francisco Paleocontinental Block with P-wave traveltime tomography, *Geophys. J. Int.,* **219**, 633–644.

Rocha, M.P., Schimmel, M. & Assumpçao, M., 2011. Upper-mantle seismic structure beneath SE and Central Brazil from P-and S-wave regional traveltime tomography, *Geophys. J. Int.,* **184**(1), 268–286.

Rodriguez, E.E. & Russo, R.M., 2020, Southern Chile crustal structure from teleseismic receiver functions: Responses to ridge subduction and terrane assembly of Patagonia, *Geosphere,* **16**(1), 378–391.

Roecker, S. & Russo, R.M., 2010. *RAMP response for 2010 earthquake*. International Federation of Digital Seismograph Networks. Other/Seismic Network. https://doi.org/10.7914/SN/XY_2010.

Rosa, J.W.C. & Fuck, R.A., 2012. Crust and upper mantle structure in central Brazil derived by receiver functions and SKS splitting analysis, *J. S. Am. Earth Sci.,* **34**, 33–46.

Rudolph, M.L., Lekić, V. & Lithgow-Bertelloni, C., 2015. Viscosity jump in Earth's mid-mantle, *Science,* **350**(6266), 1349–1352.

Ruiz, M., 2016. *Ecuador RENSIG Data*. IRIS Data Service Newsletter, N.-18,2.

Ruiz, S. & Madariaga, R., 2018. Historical and recent large megathrust earthquakes in Chile, *Tectonophysics,* **733**, 37–56.

Russo, R.M., 2004. *Studies of Crust And Upper Mantle Structure, Mantle Flow and Geodynamics of the Chile Ridge Subduction Zone*. International Federation of Digital Seismograph Networks. https://doi.org/10.7914/SN/YJ_2004

Russo, R.M., 2007. *Studies of Crust And Upper Mantle Structure, Mantle Flow and Geodynamics of the Chile Ridge Subduction Zone*. International

Federation of Digital Seismograph Networks. Other/Seismic Network. https://doi.org/10.7914/SN/Y3_2007.

Russo, R.M. & Silver, P.G., 1994. Trench-parallel flow beneath the Nazca plate from seismic anisotropy, *Science,* **263,** 1105–1111.

Russo, R.M., Silver, P.G., Franke, M., Ambeh, W.B. & James, D.E., 1996. Shear-wave splitting in northeast Venezuela, Trinidad and the Eastern Caribbean, *Phys. Earth planet. Inter.,* **95** 251–275.

Sandvol, E. & Brown, L., 2007. *SLIP - Seismic Lithospheric Imaging of the Puna Plateau*. International Federation of Digital Seismograph Networks. Other/Seismic Network. https://doi.org/10.7914/SN/X6_2007.

Schepers, G., Van Hinsbergen, D.J., Spakman, W., Kosters, M.E., Boschman, L.M. & McQuarrie, N., 2017. South-American plate advance and forced Andean trench retreat as drivers for transient flat subduction episodes, *Nat. Commun.,* **8,** 15249.

Schimmel, M., Assumpçao, M. & VanDecar, J.C., 2003. Seismic velocity anomalies beneath SE Brazil from P and S wave travel time inversions, *J. geophys. Res.,* **108**(B4).

Schmandt, B. & Humphreys, E., 2010. Seismic heterogeneity and small-scale convection in the southern California upper mantle, *Geochem. Geophys. Geosyst.,* **11,** Q05004.

Schmandt, B., Jacobsen, S.D., Becker, T.W., Liu, Z. & Dueker, K.G., 2014. Dehydration melting at the top of the lower mantle, *Science,* **344**(6189), 1265–1268.

Schmandt, B. & Lin, F.C., 2014. P and S wave tomography of the mantle beneath the United States, *Geophys. Res. Lett.,* **41**(18), 6342–6349.

Schurr, B., Rietbrock, A., Asch, G., Kind, R. & Oncken, O., 2006. Evidence for lithospheric detachment in the central Andes from local earthquake tomography, *Tectonophysics,* **415**(1–4), 203–223.

Scire, A., Zandt, G., Beck, S., Long, M. & Wagner, L., 2017. The deforming Nazca slab in the mantle transition zone and lower mantle: constraints from teleseismic tomography on the deeply subducted slab between 6° S and 32° S, *Geosphere,* **13**(3), 665–680.

Scire, A., Zandt, G., Beck, S., Long, M., Wagner, L., Minaya, E. & Tavera, H., 2016. Imaging the transition from flat to normal subduction: variations in the structure of the Nazca slab and upper mantle under southern Peru and northwestern Bolivia, *Geophys. J. Int.,* **204**(1), 457–479.

Scripps Institution of Oceanography, 1986. *IRIS/IDA Seismic Network*. International Federation of Digital Seismograph Networks. Other/Seismic Network. https://doi.org/10.7914/SN/II.

Seton, M. *et al.*, 2012. Global continental and ocean basin reconstructions since 200 Ma, *Earth-Sci. Rev.,* **113**(3–4), 212–270.

Siebert, L., Simkin, T. & Kimberly, P., 2011. *Volcanoes of the World,* University of California Press.

Silver, P.G., Beck, S.L. & Wallace, T., 1994. *Broadband Study of the Altiplano and Central Andes*. International Federation of Digital Seismograph Networks. Other/Seismic Network. https://doi.org/10.7914/SN/XE_1994.

Silver, P.G. & Chan, W.W., 1991. Shear wave splitting and subcontinental mantle deformation, *J. geophys. Res.,* **96,** 16 429–16 454.

Simmons, N.A., Myers, S.C., Johannesson, G., Matzel, E. & Grand, S.P., 2015. Evidence for long-lived subduction of an ancient tectonic plate beneath the southern Indian Ocean, *Geophys. Res. Lett.,* **42**(21), 9270–9278.

Somoza, R. & Ghidella, M.E., 2012. Late Cretaceous to recent plate motions in western South America revisited, *Earth planet. Sci. Lett.,* **331,** 152–163.

Stein, S. & Wysession, M., 2009. *An introduction to Seismology, Earthquakes, and Earth Structure*. John Wiley & Sons.

Tan, E., Gurnis, M. & Han, L., 2002. Slabs in the lower mantle and their modulation of plume formation, *Geochem. Geophys. Geosyst.,* **3**(11), 1–24.

Tao, K., Grand, S.P. & Niu, F., 2018. Seismic structure of the upper mantle beneath eastern Asia from full waveform seismic tomography, *Geochem. Geophys. Geosyst.,* **19**(8), 2732–2763.

Tassara, A. & Echaurren, A., 2012. Anatomy of the Andean subduction zone: three-dimensional density model upgraded and compared against global-scale models, *Geophys. J. Int.,* **189**(1), 161–168.

Thiede, D.S. & Vasconcelos, P.M., 2010. Paraná flood basalts: rapid extrusion hypothesis confirmed by new 40Ar/39Ar results, *Geology,* **38**(8), 747–750.

Torsvik, T.H., Müller, R.D., Van der Voo, R., Steinberger, B. & Gaina, C., 2008. Global plate motion frames: toward a unified model, *Rev. Geophys.,* **46**(3), doi:10.1029/2007RG000227.

Trenkamp, R., Kellogg , J.N., Freymueller, J.T. & Mora, H.P., 2002. Wide plate margin deformation, southern Central America and northwestern South America, CASA GPS observations *Journal of South American Earth Sciences,* **15**(2), 157–171, 10.1016/S0895-9811(02)00018-4.

Universidad de Chile, 2013. *Red Sismologica Nacional*. International Federation of Digital Seismograph Networks. Other/Seismic Network. https://doi.org/10.7914/SN/C1.

VanDecar, J.C. & Crosson, R.S., 1990. Determination of teleseismic relative phase arrival times using multi-channel cross-correlation and least squares, *Bull. seism. Soc. Am.,* **80,** 150–169.

VanDecar, J.C., James, D.E. & Assumpção, M., 1995. Seismic evidence for a fossil mantle plume beneath South America and implications for plate driving forces, *Nature,* **378**(6552), 25.

van Hunen, J., Van Den BERG, A.P. & Vlaar, N.J., 2002. On the role of subducting oceanic plateaus in the development of shallow flat subduction, *Tectonophys,* **352**(3–4), 317–333.

Vilotte, J.-P. RESIF, 2011. *Seismic network XS:CHILE MAULE aftershock temporary experiment (RESIF-SISMOB)*. RESIF - Réseau Sismologique et géodésique Français. https://doi.org/10.15778/resif.xs2010.

Vinnik, L.P., Makeyeva, L.I., Milev, A. & Usenko, Y., 1992. Global patterns of azimuthal anisotropy and deformation in the continental mantle, *Geophys. J. Int.,* **111,** 433–447.

Wagner, L., Beck, S.L. & Long, M., 2010. *PerU Lithosphere and Slab Experiment*. International Federation of Digital Seismograph Networks. Other/Seismic Network. https://doi.org/10.7914/SN/ZD_2010.

Waite, G.P., 2010. *An Integrated Analysis of Low-Frequency Seismicity at Villarrica Volcano, Chile*. International Federation of Digital Seismograph Networks. Other/Seismic Network. https://doi.org/10.7914/SN/YM_2010.

Wang, H., Wang, Y., Gurnis, M., Zahirovic, S. & Leng, W., 2018. A long-lived Indian Ocean slab: deep dip reversal induced by the African LLSVP, *Earth planet. Sci. Lett.,* **497,** 1–11.

Ward, K.M., Porter, R.C., Zandt, G., Beck, S.L., Wagner, L.S., Minaya, E. & Tavera, H., 2013. Ambient noise tomography across the Central Andes, *Geophys. J. Int.,* **194**(3), 1559–1573.

Wessel, P. & Smith, W.H., 1991. Free software helps map and display data, *EOS, Trans. Am. Geophys. Un.,* **72**(41), 441–446.

West, M. & Christensen, D., 2010. *Investigating the relationship between Pluton growth and volcanism at two active intrusions in the central Andes*. International Federation of Digital Seismograph Networks. Other/Seismic Network. https://doi.org/10.7914/SN/XP_2010.

Wölbern, I., Löbl, U. & Rumpker, G., 2014. Crustal origin of trench-parallel shear-wave fast polarizations in the Central Andes, *Earth planet. Sci. Lett.,* **392,** 230–238.

Zandt, G., 1996. *Altiplano-Puna Volcanic Complex Seismic Experiment*. International Federation of Digital Seismograph Networks. Other/Seismic Network. https://doi.org/10.7914/SN/XH_1996.

SUPPORTING INFORMATION

Supplementary data are available at *GJI* online.

Table S1. List of networks used in model. Temporary deployments are denoted by the years running in parentheses.

Figure S1. Station crustal corrections. (a) The estimated crustal thickness at each station used in our inversion. Crustal thickness estimates are derived from a combination of receiver function, reflection, and gravity studies (Assumpção *et al*. 2002, 2004, 2013; Niu *et al.* 2007; Julià *et al.* 2008; Lloyd *et al.* 2010; Tassara & Echaurren 2012; Poveda *et al.* 2015; Albuquerque *et al.* 2017; Condori *et al.* 2017; Rodriguez & Russo 2020). Crustal thicknesses range from 70 km in the high Andes to 35–40 km in the craton regions. (b) The crustal traveltime correction at each station relative to the IASPEI model with a crustal thickness of 35 km.

Figure S2. Relative traveltime residuals distributions. (a) The initial demeaned data of our traveltime residuals. (b) The same traveltime residual data of (a) after running an initial 1-D inversion. (c) The initial demeaned traveltime residual data after correcting SKS arrivals for known shear wave splitting (SWS). (d) The same traveltime data of (c) with SWS corrections after running an initial 1-D inversion. Initial data sets (a and c) include a crustal correction and are demeaned. The standard deviations are similar for both S and SKS phases and the SWS corrections makes very little difference in the relative residuals of the SKS phase.

Figure S3. The effects of shear wave splitting (SWS) traveltimes corrections on our initial (1-D ray traced) model. Column 1 shows the tomographic inversion using 1-D ray tracing with no traveltime corrections to the SKS relative residuals using SWS (variance reduction of 65.5 per cent). Column 2, the result after correcting the initial SKS traveltime residuals for SWS (variance reduction of 67.4 per cent for the 1-D ray traced model). Column 3, the difference between the two models. We note that the most significant changes to the model occur in the top and bottom-most layers, where the inversion typically puts unaccounted for anomalies. Smoothing and damping parameters were kept the same for each iteration. For all models, the black line denotes the 0.4 hit-quality contour.

Figure S4. Trade-off analysis curve. Data variance reduction versus L2 model norm for choices of smoothing and damping parameters ranging from 1 to 10 are plotted by the green circles. The solid/dashed lines correspond to constant damping (denoted as D 1–10) and smoothing (denoted as S 1–10) trends, respectively. The model with a damping parameter of 5 and smoothing parameter of 4 (yellow star) was chosen for analysis.

Figure S5. Model node distribution maps for a model with node spacing twice as large as our final model. Red dots denote model node centres and purple inverted triangles show the locations of seismic stations, for reference. (a) The top layer of our model, 60 km depth. Lateral node spacing in this layer varies from 70–230 km. (b) The bottom-most layer of our model, 1450 km depth.

Figure S6. *S*-wave tomography model depth slices from a model using double the node spacing as our final model (see Fig. S5). We note a change in the colour-scale from all other figures. For all layers the solid black line represents the 0.4 hit-quality contour. The magenta line contour denotes the Slab2 model of the Nazca slab at corresponding depths (Hayes *et al.* 2018). The green circles represent >*M* 5 earthquakes from 1960 to 1 January 2019 (NEIC-USGS, USA Earthquake catalogue 2020).

Figure S7. The effects of 3-D ray tracing on our initial model. Column 1 shows the tomographic inversion using the 1-D ray tracing with a variance reduction of 65 per cent. Column 2, the result after 1 iteration of 3-D ray tracing. Column 3, our finial model, after 6 iterations of 3-D ray tracing with a variance reduction of 70 per cent. Column 4 is the difference between the 1-D ray tracing model (column 1) and the model after 6 iterations of 3-D ray tracing (column 3). Smoothing and damping parameters were kept the same for each iteration. For all models, the black line denotes the 0.4 hit-quality contour.

Figure S8. Normalized hit-quality maps. In all panels, the black line contour marks the 0.4 normalized hit-quality. The depth of each slice is denoted in the bottom right. We use the 0.4 normalized hit-quality contour to denote the area of the model with good resolution. We do not interpret any features of the model outside this contour.

Figure S9. Standard deviations of the bootstrap resampling results. We used bootstrapping to determine uncertainties in our model and plot the standard deviations as a function of depth. Depth slices for each map are denoted in the lower right. Greyed out are regions

below 0.4 hit-quality. Areas with high station density generally have standard deviation of <1 per cent while regions with broader station density have standard deviations of up to ∼2 per cent.

Figure S10. RMS of the standard deviations from the bootstrap resampling within the 0.4 normalized hit-quality from the bootstrap resampling for each depth layer in our model. Greyed-out are the layers in our model which we do not interpret.

Figure S11. Cross sections of synthetic checkerboard tests. For all cross-sections the black solid lines outline an input anomaly of +9 per cent d*Vs*. The dashed black lines outline an input anomaly of −9 per cent d*Vs*. Our input is designed as alternating positive and negative anomalies in 3 × 3 × 3 model nodes separated by 2 model node with an input of 0 per cent d*Vs*. Note, some of our checkers appear distorted due to the cross-section choices and dilating geometry of our nodes. The thick black line indicates the 0.4 hit-quality contour.

Figure S12. Depth slices of additional checkerboard tests (2 × 2 × 2 nodes). For all maps the black solid lines outline an input anomaly of +9 per cent d*Vs*. The dashed black lines outline an input anomaly of −9 per cent d*Vs*. Our input is designed as alternating positive and negative anomalies in 2 × 2 × 2 model nodes separated by 1 model node with an input of 0 per cent d*Vs*. The thick black line indicates the 0.4 hit-quality contour.

Figure S13. Depth slices of additional checkerboard tests (5 × 5 × 5 nodes). For all maps the black solid lines outline an input anomaly of +9 per cent d*Vs*. Dashed black lines outline an input anomaly of −9 per cent d*Vs*. Our input is designed as alternating positive and negative anomalies in 5 × 5 × 5 model nodes separated by 3 model nodes with an input of 0 per cent d*Vs*. The thick black line indicates the 0.4 hit-quality contour.

Figure S14. *S*-wave tomography all model depth slices from the 3-D ray tracing results. For all layers the thick black line represents the 0.4 normalized hit-quality contour. Greyed out are regions that scored a normalized hit-quality of less than 0.4. The magenta line outlines the Slab2 model of the Nazca slab at corresponding depths (Hayes *et al.* 2018). The green circles represent >*M* 5 earthquakes from 1960 to 1 January 2019 (NEIC-USGS, USA earthquake catalogue 2020).

Figure S15. Synthetic slab tear tests. The black contour denotes the location of the synthetic input anomaly of +9 per cent d*Vs* representing the Nazca slab. (a) Shows the recovered slab anomaly (coloured scale) with a gap in the input anomaly from 505 to 660 km depth beneath the northern portion of the Bolivian orocline. (b) The recovered slab anomaly (coloured scale) with a gap in the input anomaly from 280 to 410 km depth beneath the Sierras Pampeanas. Plotted above the model cross-sections is topography. The yellow inverted triangle denotes the location of the trench on the map and corresponding cross-sections. Our input synthetic slab anomaly comes from the Nazca slab model of Portner *et al.* (2020) with the addition of slab gaps.

Figure S16. Slab gap comparison cross-sections. For all cross-sections (a–d) the Slab2 model of the Nazca slab at corresponding depths is denoted by the thicker contour (Hayes *et al.* 2018). The circles represent >*M* 5 earthquakes from 1960 to 1 January 2019 (NEIC-USGS, USA Earthquake catalogue 2020). The inverted triangle denotes the location of the trench on the inset map and corresponding cross-sections. Cross-sections (a) and (c) show the cross-sections through our final *S*-wave tomography model. The solid black line represents the 0.4 hit-quality contour. Greyed out are regions that scored a hit-quality of less than 0.4. Cross-sections (b) and (d) show the equivalent cross-sections through the SAM_P_2019 (Portner *et al.* 2020) model. In these cross-sections the thick solid

black line represents their 0.2 hit-quality contour, where authors delimit resolved regions of their model (Portner *et al.* 2020). Greyed out are regions that scored a hit-quality of less than 0.2.

Figure S17. Plate reconstruction of the southeastern Pacific at 60 Ma. Arrows represent corresponding plate motions. After Gianni *et al.* (2018).

Please note: Oxford University Press is not responsible for the content or functionality of any supporting materials supplied by the authors. Any queries (other than missing material) should be directed to the corresponding author for the paper.